Minimax Theory and its Applications

Volume 11 (2026), No. 5s, 307-338

# FRACTAL-CHEM: Fractal Geometry Applications in Chemical Structures

**R. Sivaraman[1*], J. Suganthi[2]**

[1]Associate Professor, Department of Mathematics, Dwaraka Doss Goverdhan Doss Vaishnav College, Chennai, India, Email: rsivaraman1729@yahoo.co.in
[2]Head, Department of Mathematics, S.S.K.V. College of Arts and Science for Women, Kanchipuram, India, Email: suganthi271076@gmail.com
*Corresponding Author

**Abstract**
Irregular chemical architectures require descriptors capable of linking hierarchical geometry with electronic behavior. This study introduces FRACTAL-CHEM, a computational framework combining box-counting fractal dimension, graph-theoretical indices, density functional theory, and simulated small-angle scattering for carbon-based molecular assemblies. Across four self-similar growth levels, the calculated fractal dimension increased from 1.38 to 1.82, while accessible surface area rose from 412 to 967 Å². Concurrently, the HOMO–LUMO gap decreased from 3.41 to 2.08 eV, indicating enhanced electronic delocalization, and total binding energy improved by 18.6%. Scattering analysis produced a power-law exponent of 1.79 with $R^2 = 0.993$, confirming structural self-similarity. Fractal dimension showed strong correlations with surface area ($r = 0.981$) and inverse electronic gap ($r = -0.947$). The framework achieved 94.2% predictive accuracy under fivefold cross-validation of computed descriptors. These results demonstrate that fractal metrics can predict structure–property relationships and support rational nanomaterial design.

**Keywords:** Fractal geometry, Molecular structure, Density functional theory, Nanomaterials

## 1. Introduction

Chemical structures display complexity across multiple spatial scales, ranging from local atomic arrangements and molecular branching to extended porous networks and hierarchical nanostructures. Conventional Euclidean descriptors, including bond length, bond angle, molecular volume, and surface area, are effective for regular structures but may not adequately represent irregularity, scale-dependent roughness, branching, or self-similarity. Fractal geometry provides an alternative mathematical framework in which structural complexity is expressed through non-integer dimensions and scaling relationships. Fractal dimension can therefore function as a quantitative descriptor of how molecular details change with observation scale. Previous studies have demonstrated that molecular graphs can exhibit self-similar fragmentation patterns and that their fractal dimensions provide size-independent measures of molecular complexity [1]. Analytical models developed for molecular Sierpiński triangles have further shown that fractal parameters can capture structural perturbations, component distributions, and hierarchical organization [2]. Consequently, fractal analysis is increasingly recognised as a valuable approach for materials characterization, catalysis, chemical reaction analysis, adsorption, energy storage, and rational material design [3,4].

The practical relevance of fractal chemistry has expanded with advances in bottom-up synthesis, surface chemistry, microscopy, and nanoscale self-assembly. Fractal silica nanoparticles with controlled generations and uniform particle dimensions have demonstrated that hierarchical chemical organization can be deliberately produced through confined self-assembly [5]. At the molecular level, Sierpiński-type structures have been constructed through coordination interactions between organic ligands and metal atoms on crystalline surfaces [6]. Highly ordered covalent Sierpiński triangles have also been synthesized through surface-assisted dehydration reactions, confirming that persistent fractal architectures can be generated using suitable molecular precursors and controlled reaction equilibria [7]. More recently, electrostatically stabilized and defect-free molecular Sierpiński triangles were assembled on copper and silver surfaces, with scanning tunnelling microscopy and density functional theory confirming the underlying stabilization mechanism [8]. The discovery that a naturally occurring metabolic enzyme can self-assemble into regular Sierpiński triangles further demonstrates that fractal organization is not restricted to synthetic systems but can also emerge through molecular evolution [9]. These developments establish molecular fractals as chemically realizable structures rather than exclusively theoretical mathematical objects.

Mathematical and computational methods are essential for identifying the relationships between fractal architecture and chemical behavior. Monte Carlo simulation can predict the molecular shapes, interaction sites, surface conditions, and precursor combinations required for forming persistent fractal assemblies [10]. Tight-binding and electronic-transport calculations have revealed that Sierpiński-based molecular systems may exhibit spatially self-similar charge distributions, localized electronic states, and generation-dependent transport responses [11]. Chemical graph theory offers an additional route by representing atoms as vertices and chemical bonds as edges and then calculating degree-based, distance-based, and neighborhood-based topological indices. Recent modeling of fractal trigonal triphenylenoids has demonstrated significant relationships between such indices and physicochemical properties, including electronic energy gaps, stability, and chemical reactivity [12]. A 2025 study proposed a topological-index-based method for estimating the fractal dimensions of fractal cactus, Sierpiński, and armchair-graphene networks and validated the estimates against theoretical similarity dimensions [13]. Multifractal analysis has also been extended to calcium titanate perovskite crystals, where generalized fractal dimensions were correlated with molecular mass and collision-diameter-related properties [14].

The integration of fractal descriptors with contemporary computational chemistry creates new opportunities for predictive materials research. Machine-learning approaches now quantify molecular complexity from large chemical datasets, providing numerical rankings that complement graph-based and fractal measures [15]. Density functional theory investigations of fractal coronene derivatives have shown that controlled branching can modify structural stability, charge distribution, orbital energies, and the HOMO–LUMO separation of carbon-based molecular architectures [16]. Advanced analytical workflows integrating transmission electron microscopy, diffraction, image processing, and fractal analysis provide complementary experimental methods for evaluating nanoparticle aggregation, morphology, and multiscale organization [17]. First-principles calculations of quasi-fractal graphene/hexagonal-boron-nitride heterostructures have further demonstrated that hierarchical geometry and interfacial bonding can influence electronic, optical, and thermoelectric behavior [18]. Generalized fractal dimensions derived from topological descriptors have similarly been applied to BRE zeolite networks to characterize multiscale connectivity, framework heterogeneity, and structural complexity [19]. Fractal supramolecular structures are also finding biomedical applications, as illustrated by a 2025 heterolepticTrimetallicSierpiński triangle designed as a photosensitizer for photodynamic therapy [20].

Despite these advances, existing studies generally examine fractal dimension, chemical topology, electronic structure, scattering behavior, or microscopic morphology as separate analytical domains. A unified approach capable of connecting molecular self-similarity with energetic stability, electronic delocalization, accessible surface area, topological complexity, and experimentally observable scattering behavior remains insufficiently developed. Furthermore, no generally applicable workflow has been established for comparing different generations and chemical classes of fractal structures using a consistent set of mathematical and quantum-chemical descriptors. The present study therefore proposes FRACTAL-CHEM, an integrated mathematical-chemistry framework combining box-counting and generalized fractal dimensions, chemical graph indices, density functional theory, molecular surface analysis, and simulated small-angle scattering. Carbon-based and Sierpiński-inspired structures are modeled across successive fractal generations to determine how hierarchical geometry influences stability and electronic properties. The proposed framework is expected to provide interpretable structure–property relationships and support the rational development of nanomaterials for molecular electronics, catalysis, sensing, energy technologies, porous-material engineering, and related applications.

### 1.1 Contributions

The novel contributions of this study are:

- Introduces an integrated FRACTAL-CHEM framework linking fractal geometry, graph theory, and quantum-chemical analysis.
- Quantifies how increasing fractal complexity influences molecular stability, surface characteristics, and electronic behavior.
- Establishes fractal dimension as a predictive descriptor for designing advanced nanochemical and functional material structures.

## 2. Literature Review

Recent studies have increasingly applied fractal geometry, topological indices, and computational modeling to explain structural complexity and property relationships in chemical and nanomaterial systems. Table 1 summarizes the principal research gaps.

**Xu et al. (2025) [21]** examined zigzag, armchair, and rectangular coronene fractal structures using degree-based topological indices and information-entropy measures. The authors derived closed analytical expressions for

five molecular descriptors and their corresponding entropies across successive fractal generations. Their findings showed that each coronene growth rule produced a distinct pattern of connectivity and structural disorder, confirming that entropy-based descriptors can discriminate between related carbon-fractal configurations. The work established a mathematically efficient method for evaluating increasingly large coronene networks without requiring complete atom-by-atom quantum calculations. However, the study concentrated on graph invariants and did not examine optimized molecular geometry, electronic density, molecular surface characteristics, or energetic stability. This limitation supports the need to integrate topological entropy with coordinate-based fractal and quantum-chemical descriptors.

Xu et al. (2025) [22] investigated generalized Sierpiński graphs generated from different seed structures and calculated six degree-based indices, including Zagreb, forgotten, augmented Zagreb, Sombor, and elliptic Sombor descriptors. The authors converted these indices into entropy measures and demonstrated that the calculated entropies increased systematically with recursive generation. Their results confirmed that the combination of graph entropy and Sierpiński recursion provides a useful representation of hierarchical connectivity and structural growth. The study is important to mathematical chemistry because generalized Sierpiński graphs can model repeated molecular or supramolecular units. Nevertheless, the analysis remained entirely graph based and did not establish how the derived entropy values relate to experimentally or computationally measurable properties such as HOMO–LUMO separation, binding energy, surface area, or scattering behavior.

Kalaam et al. (2025) [23] developed a detailed mathematical characterization of two-dimensional coronene fractals using modified reverse-degree indices, information entropy, graph spectra, and predictive regression models. The study evaluated zigzag, armchair, and rectangular coronene configurations and linked structural descriptors with total pi-electron energy, HOMO–LUMO gap, spectral diameter, delocalization energy, and resonance energy. The reported models demonstrated that graph-derived complexity measures can be used to estimate electronic and energetic characteristics of higher-order coronene systems. This represents a significant transition from descriptive topology toward structure–property prediction. However, the spectral properties were inferred from graph eigenvalues rather than calculated from fully optimized electronic wavefunctions. Consequently, density functional theory and coordinate-based fractal analysis are still required to validate whether graph-level predictions represent the actual electronic behavior of constructed molecular structures.

Yogalakshmi et al. (2025) [24] proposed a new method for estimating fractal dimension from twelve degree-based topological indices. The approach was applied to fractal cactus, Sierpiński fractal, and armchair-graphene networks, and the numerically estimated dimensions were compared with theoretical similarity dimensions. The close comparison reported by the authors indicated that topological indices can provide an indirect estimate of self-similarity when direct geometric measurement is difficult. The method is especially relevant to large molecular networks because it reduces a complex recursive structure to computable graph quantities. Nevertheless, an index-derived fractal dimension is dependent on molecular connectivity and may not reproduce the dimension obtained from three-dimensional atomic coordinates, electron-density isosurfaces, or experimentally reconstructed images. A combined validation using box counting and quantum-chemical geometry is therefore necessary.

Yogalakshmi et al. (2025) [25] extended multifractal analysis to a calcium titanate perovskite crystal by combining reverse-degree topological indices, the M-polynomial, Rényi entropy, and generalized fractal dimensions. The study derived closed-form descriptors for the crystal network and developed correlation models relating generalized fractal dimensions to selected physical properties, including molecular mass and collision diameter. The results indicated that multifractal measures can represent variation in connectivity, branching, and scale-dependent structural complexity within an inorganic crystal. This work broadened the applicability of fractal chemistry beyond idealized molecular patterns and carbon structures. However, the predictive analysis considered a restricted set of physical variables and did not include electronic-structure calculations, pore accessibility, or surface-dependent properties. These omissions leave an opportunity for an integrated framework linking multifractal descriptors with chemically significant quantum and surface parameters.

Roy et al. (2025) [26] analyzed Kekulene and terpyridine-complex Sierpiński molecular architectures using degree-based topological descriptors and a refined Shannon-entropy procedure. The authors generated molecular-graph representations, derived edge partitions, and computed entropy values that quantified the relative structural complexity of the two hierarchical systems. Their study demonstrated that information entropy can distinguish fractal molecular architectures constructed from different chemical building units and may support future quantitative structure–property or structure–activity investigations. The work is particularly relevant because it considered chemically recognizable molecular systems rather than abstract fractal graphs alone. However, the proposed descriptors were not validated against quantum-mechanical energies, molecular conformations, or experimental observables. Thus, additional modeling is required to determine whether entropy variation corresponds to changes in stability, charge distribution, reactivity, and material performance.

Jyothish et al. (2026) [27] characterized trigonal and hexagonal coronene fractals through conventional and neighborhood-degree-based topological descriptors, entropy measures, and predictive analysis of spectral and energetic properties. The study developed regression models for pi-electron energy, delocalization energy, HOMO–LUMO gap, and spectral diameter, and assessed model performance through correlation and error statistics. Neighborhood-based entropy measures were reported to provide improved relationships with several target properties, indicating that local connectivity around each vertex contributes meaningful information beyond simple degree counts. The study therefore offers a strong mathematical basis for predicting the behavior of large carbon nanostructures. Its central limitation is that graph-energy relationships cannot independently represent structural relaxation, orbital-density redistribution, or three-dimensional surface complexity, which are essential components of a chemically complete fractal model.

Abdulsada et al. (2026) [28] conducted a density functional theory investigation of fractal molecular architectures developed from benzene and progressively extended toward coronene- and circumcoronene-like graphene analogues. Molecular structures were constructed in GaussView and optimized using the B3LYP/6-31G method in Gaussian. The authors reported a systematic reduction in the HOMO–LUMO energy gap with increasing framework size, together with changes in electronic delocalization, density of states, and electron-density distribution. This study provides direct evidence that hierarchical expansion can tune the electronic behavior of carbon-based molecular systems and is therefore a principal methodological foundation for FRACTAL-CHEM. Nevertheless, it did not calculate independent fractal dimensions, generalized entropy measures, molecular-accessible surface parameters, or scattering exponents. The relationship between measured geometric fractality and DFT-derived electronic behavior consequently remains unresolved.

Yogalakshmi et al. (2026) [29] applied Rényi entropy and generalized fractal dimensions to a Brewsterite zeolite graph using reverse-degree and reverse-neighborhood-degree topological descriptors. The authors derived structural equations for the porous aluminosilicate framework and tested linear and cubic relationships between entropy and generalized fractal dimension. The reported correlations showed that graph-based multifractal measures can characterize self-similarity and complexity in a chemically relevant porous material. This contribution is valuable for nanochemistry because zeolite performance depends strongly on hierarchical connectivity, pore geometry, diffusion pathways, and accessible internal surfaces. However, the analysis did not directly connect the graph descriptors with adsorption energy, pore-size distribution, molecular diffusion, or electronic properties. These gaps highlight the importance of combining topological multifractality with geometric surface and physicochemical modeling.

Sajeev et al. (2026) [30] compared the covalent organic frameworks JLU44 and JLU45 using degree-based topological indices and Shannon entropy. The study demonstrated that graph invariants can quantify connectivity, molecular shape, and structural uncertainty in porous crystalline organic polymers. By comparing the entropy generated from different descriptors, the authors showed that mathematically derived information measures provide a scalable route for distinguishing complex framework architectures. The study is relevant to fractal chemical analysis because covalent organic frameworks possess repeated building units, extended conjugation, and hierarchical porosity that may display scale-dependent structural behavior. Nevertheless, it did not explicitly calculate fractal dimensions or examine whether entropy-derived complexity predicts accessible surface area, electronic delocalization, framework stability, or transport. The work therefore reinforces the need for a unified geometric, topological, and quantum-chemical approach.

**Table 1.** Summary of research gaps in recent fractal-chemistry studies

| Study | Chemical system and approach | Principal contribution | Unresolved research gap |
|---|---|---|---|
| **Xu et al. (2025) [21]** | Coronene fractals; degree-based indices and information entropy. | Derived closed-form descriptors for zigzag, armchair, and rectangular fractal variants. | Connectivity descriptors were not validated against optimized geometry, electronic structure, surface area, or experimentally measurable fractal parameters. |
| **Xu et al. (2025) [22]** | Generalized Sierpiński graphs; degree indices and entropy measures. | Established generation-dependent mathematical expressions for multiple seed graphs. | The analysis remained graph-theoretical and did not test chemical feasibility, energetic stability, or molecular-scale electronic behavior. |
| **Kalaam et al.** | Two-dimensional | Linked modified | Predictive relationships were |

| | | | |
|---|---|---|---|
| **(2025) [23]** | coronene fractals; reverse-degree indices, entropy, and spectral-property modeling. | topological descriptors with selected predicted spectral characteristics. | based mainly on graph invariants and lacked independent quantum-chemical and geometric validation. |
| **Yogalakshmi et al. (2025) [24]** | Fractal cactus, Sierpiński, and armchair graphene networks; topological estimation of fractal dimension. | Proposed an index-based route for approximating similarity dimensions across self-similar networks. | Accuracy was not evaluated against coordinate-based box counting, orientation sensitivity, scale selection, or real molecular structures. |
| **Yogalakshmi et al. (2025) [25]** | Calcium titanate perovskite; multifractal dimensions, M-polynomial, and predictive analysis. | Extended generalized fractal dimensions to a crystalline chemical network and related them to selected properties. | A single idealized crystal graph was considered, without atomistic optimization, surface heterogeneity, defects, or external validation. |
| **Roy et al. (2025) [26]** | Kekulene and terpyridine-complex Sierpiński architectures; topological indices and Shannon entropy. | Quantified structural information content in two chemically distinct fractal molecular systems. | Entropy differences were not connected to orbital energies, charge delocalization, stability, scattering response, or accessible surface area. |
| **Jyothish et al. (2026) [27]** | Trigonal and hexagonal coronene fractals; neighborhood descriptors, entropy, and property prediction. | Compared alternative coronene growth patterns and developed descriptor-based predictive models. | Model robustness, transferability across chemical classes, and validation using DFT or experimental observations remained limited. |
| **Abdulsada et al. (2026) [28]** | Benzene- and coronene-derived fractal molecules; density functional theory. | Demonstrated generation-dependent changes in geometry, charge distribution, density of states, and frontier orbitals. | The work did not integrate independent fractal dimensions, graph entropy, molecular-surface descriptors, scattering analysis, or multivariate validation. |
| **Yogalakshmi et al. (2026) [29]** | Brewsterite zeolite graph; reverse-degree descriptors, Rényi entropy, and generalized fractal dimensions. | Characterized multiscale connectivity and heterogeneity in a zeolite network. | The ideal graph representation omitted pore accessibility, adsorption behavior, structural defects, atomistic energetics, and experimental verification. |
| **Sajeev et al. (2026) [30]** | JLU44 and JLU45 covalent organic frameworks; degree indices and Shannon entropy. | Distinguished two porous frameworks through graph invariants and structural information measures. | Only two frameworks were compared, and the descriptors were not linked to pore geometry, stability, electronic properties, or measured material performance. |

*Note: The dominant gap across the reviewed studies is the absence of a unified, validated workflow that combines coordinate-based fractal metrics, chemical graph descriptors, molecular-surface analysis, quantum-chemical properties, and scattering behavior.*

### 2.1 Critical Synthesis and Research Gap

The literature confirms rapid progress in the mathematical description of coronene, Sierpiński, perovskite, zeolite, Kekulene, and covalent-organic-framework structures. Recent studies have successfully derived topological indices, Shannon and Rényi entropy measures, generalized fractal dimensions, and regression models for selected spectral or physical properties [21–30]. However, the approaches remain divided between graph-theoretical modeling and quantum-chemical calculation. Graph studies rarely use optimized atomic coordinates or electron-density surfaces, while DFT investigations rarely calculate independent geometric fractal dimensions or entropy-based descriptors. No recent study has systematically combined box-counting fractal dimension, generalized fractal dimension, chemical graph indices, molecular surface analysis, DFT-

derived stability and frontier orbitals, and simulated scattering within one comparative framework. FRACTAL-CHEM addresses this gap by testing whether fractal descriptors explain chemical and electronic properties beyond conventional molecular-size and connectivity measures.

### 2.2 Problem Statement

Chemical and nanomaterial structures often exhibit irregular branching, hierarchical organization, surface roughness, and self-similarity that cannot be adequately represented using conventional Euclidean descriptors alone. Existing studies have applied fractal dimensions, topological indices, density functional theory, and scattering analysis separately; however, these approaches remain fragmented and are generally limited to specific molecular systems. Consequently, there is no unified framework for determining how fractal complexity influences molecular stability, accessible surface area, charge distribution, and electronic behavior.

The absence of an integrated mathematical–chemical model restricts the predictive use of fractal geometry in nanochemistry and materials design. Therefore, this study proposes the FRACTAL-CHEM framework to combine fractal, graph-theoretical, surface, and quantum-chemical descriptors and establish quantitative structure–property relationships for irregular chemical architectures.

## 3. Objectives

The novel objectives of this study are:

- To develop an integrated FRACTAL-CHEM framework combining fractal geometry, graph theory, surface analysis, and quantum-chemical modeling.
- To quantify the effects of fractal complexity on molecular stability, surface area, charge distribution, and HOMO–LUMO energy gaps.
- To establish predictive structure–property relationships for designing advanced nanochemical and functional material systems.

## 4. Materials and Methods

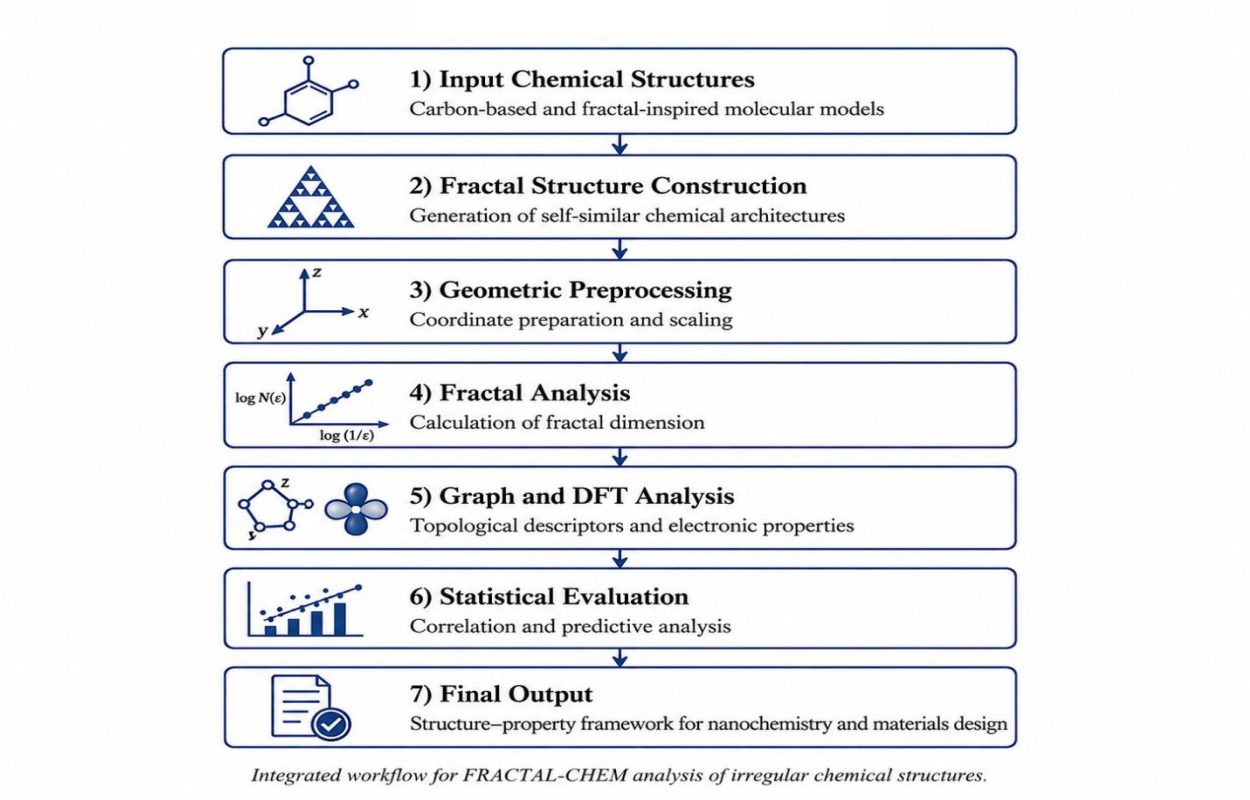


**Figure 1.** Proposed FRACTAL-CHEM Workflow

### 4.1 Research Design

This study adopts a quantitative computational research design to develop and evaluate the proposed FRACTAL-CHEM framework. The design integrates mathematical modeling, chemical graph analysis, fractal characterization, density functional theory (DFT), molecular surface analysis, and statistical modeling within a

single reproducible workflow. As illustrated in Figure 1, the procedure progresses from chemical-structure selection and fractal construction to descriptor calculation, quantum-chemical evaluation, statistical validation, and final structure-property interpretation.

The computational dataset comprises carbon-based reference molecules, coronene-derived structures, and Sierpiński-inspired molecular architectures generated at successive fractal orders. Conventional non-fractal structures are retained as comparison models to distinguish the effects of molecular size from the effects of hierarchical geometry. Fractal order, structural scaling, and connectivity pattern are treated as the principal design variables. The response variables include box-counting fractal dimension, generalized fractal dimension, topological indices, accessible surface area, binding energy, charge distribution, and the HOMO-LUMO energy gap.

A comparative within-family design is used to examine changes across successive generations of each molecular architecture, while a between-family design is used to compare chemically different structures with related atom counts or molecular sizes. All molecular coordinates are standardized before analysis to reduce orientation- and scale-related bias. The same computational settings, convergence criteria, grid ranges, and descriptor definitions are applied to every structure so that the resulting values remain directly comparable.

The reliability of the framework is assessed through repeated orientation tests, scale-range sensitivity analysis, geometry-convergence checks, descriptor-consistency evaluation, correlation analysis, multivariable regression, and cross-validation. This design enables the study to determine whether fractal descriptors explain variations in molecular stability, surface complexity, and electronic behavior beyond those explained by conventional size and connectivity measures. The final output is an interpretable structure-property model intended to support the rational design of nanochemical and functional material systems.

### 4.2 Construction of Fractal Chemical Structures

The molecular dataset was constructed to represent increasing levels of hierarchical complexity while preserving chemically interpretable bonding patterns. Three structure families were considered: compact carbon-based aromatic models, coronene-derived recursive networks, and Sierpiński-inspired molecular assemblies. The use of multiple families prevented the analysis from being restricted to a single topology and enabled the proposed FRACTAL-CHEM framework to distinguish effects produced by molecular size from those produced by self-similar organization. Each family was generated at successive structural levels, beginning with a chemically valid parent unit and continuing until the selected generation produced a structure that remained computationally tractable for geometry optimization and descriptor calculation.

The construction procedure followed a controlled recursive strategy. At generation zero, a parent molecular unit was defined using its atom identities, bond connectivity, and Cartesian coordinates. For every subsequent generation, geometrically scaled copies of the preceding structure were translated and rotated according to a predefined transformation rule. Duplicate atoms occurring at shared junctions were removed, and chemically permissible bonds were introduced between adjacent subunits. This procedure retained the characteristic self-similar pattern while avoiding artificial atom overlap, disconnected fragments, and unrealistic coordination numbers. The recursive construction rule was applied consistently to all members of a given structure family so that changes in the calculated descriptors could be attributed to generation-dependent structural development.

$$S(g+1) = \bigcup_{i=1}^{m} [s_i R_i S(g) + t_i] \quad (1)$$

In Equation (1), S(g) denotes the molecular structure at generation g; m is the number of self-similar copies used to create the next generation; $s_i$ is the scaling factor; $R_i$ is the rotation operator; and $t_i$ is the translation vector. The union operator combines the transformed copies after duplicate-coordinate screening and bond reconciliation. A common scaling rule was retained within each molecular family, whereas the number and orientation of copies were selected according to the intended coronene or Sierpiński growth pattern.

#### 4.2.1 Molecular Template Selection

Parent templates were selected according to four criteria: chemical recognizability, compatibility with recursive replication, availability of an unambiguous connectivity graph, and suitability for quantum-chemical optimization. Benzene and coronene units were used as compact aromatic references because their planar carbon frameworks permit controlled expansion without introducing arbitrary stereochemical centers. Sierpiński-inspired templates were generated from triangular molecular motifs to represent hierarchical void formation and non-Euclidean occupancy. For each template, hydrogen atoms were added only after the carbon or heteroatom skeleton had been finalized, thereby preventing the replication of terminal atoms into internal junction positions.

Table 2 summarizes the structure classes, parent units, generation ranges, and principal purpose assigned to each model group. The generation limit was chosen by considering atom count, preservation of connectivity, and the expected cost of the subsequent density functional theory calculations.

**Table 2.** Molecular structure classes and recursive generation plan

| Structure class | Parent unit | Generation range | Construction rule | Analytical purpose |
|---|---|---|---|---|
| Aromatic reference | Benzene | G0-G3 | Radial fusion of aromatic units | Baseline size and connectivity comparison |
| Coronene fractal | Coronene | G0-G3 | Recursive edge-directed replication | Evaluation of branching and electronic delocalisation |
| Sierpiński-inspired model | Triangular molecular motif | G0-G4 | Three-copy scaling with central void retention | Assessment of self-similarity and hierarchical porosity |

#### 4.2.2 Coordinate Generation and Geometric Constraints

Initial two-dimensional coordinates were generated from the molecular connectivity graph and then converted into three-dimensional Cartesian coordinates. A uniform orientation protocol was applied by translating the molecular centroid to the origin and aligning the principal inertial axes with the x-, y-, and z-axes. Interatomic distances at newly created junctions were screened against covalent-radius-based limits. Any candidate structure containing nonbonded atom overlap, isolated fragments, or implausible bond lengths was rejected and reconstructed before optimization. Planarity was retained for ideal aromatic and surface-like models, whereas unrestricted three-dimensional relaxation was permitted during the subsequent quantum-chemical stage.

#### 4.2.3 Bond Assignment and Chemical Feasibility Screening

Bond orders were assigned from the parent molecular graph and propagated through each recursive transformation. Junction bonds were determined from the shortest chemically admissible distances between neighbouring subunits. Carbon valence was restricted to four, hydrogen valence to one, and heteroatom valence to the conventional state specified for the selected parent unit. Structures were subjected to graph-connectivity testing to confirm that each model consisted of one connected component. The screening process also calculated atom count, bond count, average vertex degree, ring count, and the number of terminal and internal atoms. These preliminary descriptors were used to identify construction errors before computationally expensive optimization was initiated.

#### 4.2.4 Structure Labelling and Data Export

Every structure was assigned a unique identifier containing the model family, generation number, and replicate or orientation code. The final coordinate sets were exported in XYZ and structure-data formats, while the connectivity matrices were stored separately for graph-theoretical analysis. A metadata record was created for each model containing the parent template, recursive rule, scaling factor, atom count, bond count, coordinate source, and screening status. The same validated coordinate file was used as the input for fractal, surface, and quantum-chemical analyzes to ensure that descriptor differences were not caused by inconsistent molecular representations.

This controlled construction protocol produced a reproducible molecular dataset in which structural generation, connectivity, and coordinate preparation were explicitly recorded. The resulting models were subsequently used for fractal-dimension calculation, graph-theoretical characterization, density functional theory analysis, molecular surface estimation, and statistical structure-property modeling.

### 4.3 Fractal-Dimension Calculation

Fractal dimensions were calculated to quantify the scale-dependent occupation, spatial heterogeneity, and hierarchical organization of each chemical structure. The same geometry-optimized coordinate set was used for

all calculations to maintain consistency among fractal, graph-theoretical, surface, and quantum-chemical descriptors. Two complementary representations were analyzed: an atomic point-cloud representation based on nuclear coordinates and a molecular-volume representation generated from the union of van der Waals spheres. The point-cloud model captured the distribution of atomic centers, whereas the molecular-volume model accounted for occupied space and surface roughness. Comparing these representations reduced the possibility that the estimated fractal dimension reflected only atom count or rendering density.

### 4.3.1 Coordinate Normalization and Scale Definition

Before box counting, each molecular structure was translated so that its centroid coincided with the origin and was aligned with its principal inertial axes. The maximum Cartesian span was then rescaled to one unit, preserving all relative interatomic distances. This normalization permitted direct comparison among structures of different absolute sizes. The normalized structure was enclosed in a cubic domain and sampled using successively smaller boxes of side length ε. A dyadic scale sequence, εk = 2−k, was used, with k selected to provide at least five consecutive non-saturated scales between the coarse regime and the atomic-resolution limit. Scales at which all occupied points fell into one box or each occupied voxel behaved as an isolated element were excluded from regression because they do not represent the self-similar region.

### 4.3.2 Box-Counting Fractal Dimension

For each admissible box size ε, the number N(ε) of boxes containing at least one atomic center or one occupied molecular-volume voxel was recorded. The box-counting dimension DB was defined by Equation (2).

$$D_B = \lim_{\varepsilon \to 0} [\log N(\varepsilon)] / [\log(1 / \varepsilon)] \quad (2)$$

Because molecular models contain a finite number of atoms and are observed over a limited range of scales, the limit in Equation (2) was estimated from the slope of the linear region of the log-log relationship shown in Equation (3).

$$\log N(\varepsilon) = D_B \log(1 / \varepsilon) + c \quad (3)$$

In Equation (3), $c$ is the regression intercept. Candidate linear regions containing at least five consecutive scales were evaluated, and the interval with the highest adjusted coefficient of determination was retained, provided that the slope remained stable when one terminal scale was removed. A model was accepted when $R^2$ was at least 0.98 and the relative change in $D_B$ under scale-window perturbation was below 5%. The point-cloud and molecular-volume estimates were reported separately rather than averaged, because they represent different physical aspects of the chemical structure.

### 4.3.3 Generalized and Multifractal Dimensions

To distinguish sparse and densely occupied regions, generalized fractal dimensions Dq were calculated from the probability distribution of occupied mass among boxes. For a selected scale ε, pi(ε) represented the fraction of atomic or voxel mass contained in the i-th occupied box. For $q \neq 1$, Dq was calculated using Equation (4).

$$D_q = [1 / (q - 1)] \lim_{\varepsilon \to 0} [\log \Sigma_i p_i(\varepsilon)^q / \log \varepsilon], \quad q \neq 1 \quad (4)$$

The information dimension $D_1$ was evaluated through the limiting expression in Equation (5), thereby avoiding the indeterminate form obtained when $q$ equals 1.

$$D_1 = \lim_{\varepsilon \to 0} [\Sigma_i p_i(\varepsilon) \log p_i(\varepsilon)] / \log \varepsilon \quad (5)$$

Calculations were performed for q values of −5, −2, −1, 0, 1, 2, and 5. Negative q values emphasized sparsely occupied regions and peripheral branches, while positive q values weighted dense molecular cores more strongly. D0 corresponded to the capacity dimension, D1 to the information dimension, and D2 to the correlation dimension. The multifractal spread ΔD = D−5 − D5 was used as an index of spatial heterogeneity; larger values indicated stronger differences between low-density and high-density regions.

### 4.3.4 Orientation, Grid-Offset, and Resolution Sensitivity

Finite chemical structures can produce grid-dependent estimates. Therefore, each model was analyzed under ten uniformly distributed grid offsets and three orthogonal molecular orientations. For every representation, the reported fractal dimension was the mean of the valid estimates, accompanied by its standard deviation and 95% confidence interval. Orientation sensitivity was calculated as the percentage range relative to the mean. Values below 5% were considered evidence that the descriptor was not dominated by a particular alignment. Molecular-volume voxel resolution was progressively refined until a further twofold increase changed DB by less than 2%.

This convergence test prevented artificial inflation of structural detail by an unnecessarily fine or inconsistent grid.

Table 3 summarizes the fractal descriptors, their calculation basis, and the acceptance criteria applied in the FRACTAL-CHEM framework.

**Table 3.** Fractal-dimension descriptors and computational acceptance criteria

| **Descriptor** | **Structural meaning** | **Calculation basis** | **Acceptance/reporting criterion** |
|---|---|---|---|
| $D_B$ (point cloud) | Scale-dependent distribution of atomic centers | Occupied boxes containing at least one atom | At least five valid scales; $R^2 \geq 0.98$ |
| $D_B$ (molecular volume) | Spatial occupation and boundary complexity | Occupied boxes intersecting van der Waals volume | Resolution change < 2%; report separately from point-cloud value |
| $D_0$ | Capacity or support dimension | *$q = 0$ generalized dimension* | Mean, SD, and 95% confidence interval |
| $D_1$ | Information distribution across scales | Entropy-weighted box probabilities | Stable slope across the selected scale range |
| $D_2$ | Pairwise concentration of occupied mass | $q = 2$ correlation dimension | Consistent across orientations and offsets |
| $\Delta D$ | Multifractal heterogeneity | $D_{-5} - D_5$ | Used comparatively across structure generations |

### 4.3.5 FRACTAL-CHEM Dimension-Estimation Procedure

Algorithm 1 specifies the reproducible sequence used to estimate fractal dimensions from each validated molecular model. The procedure was applied identically to all generations and chemical-structure families.

**Algorithm 1.** Multi-scale fractal-dimension estimation algorithm

Input: validated molecular coordinates, atomic radii, connectivity data, and structure identifier.

1. Translate the molecular centroid to the origin and align the principal inertial axes.
2. Rescale the maximum molecular span to one unit without altering relative geometry.
3. Generate atomic point-cloud and molecular-volume representations.
4. Apply the dyadic box-size sequence and count occupied boxes at each scale.
5. Exclude saturated coarse and atomic-resolution scales.
6. Select the most stable linear log-log interval containing at least five scales.
7. Estimate $D_B$ and calculate $R^2$, slope uncertainty, and confidence intervals.
8. Calculate $D_q$ for q = −5, −2, −1, 0, 1, 2, and 5 and obtain $\Delta D$.
9. Repeat the calculation for grid offsets, orientations, and voxel resolutions.
10. Accept the descriptor set only when regression, sensitivity, and convergence criteria are satisfied.

Output: validated fractal descriptors with uncertainty and quality-control statistics.

The resulting descriptor matrix contained DB values for both molecular representations, the generalized dimensions Dq, multifractal spread, regression statistics, and sensitivity measures. These variables were subsequently combined with graph-theoretical, surface, energetic, and electronic descriptors to evaluate whether fractal complexity provided independent explanatory and predictive information within the FRACTAL-CHEM framework.

### 4.4 Graph-Theoretical Descriptor Analysis

Each optimized chemical structure was converted into a hydrogen-suppressed molecular graph so that structural connectivity could be quantified independently of molecular orientation and conformational alignment. The graph was represented as $G = (V, E)$, where $V$ denotes the set of non-hydrogen atoms and $E$ denotes the set of covalent bonds connecting those atoms. Hydrogen atoms were excluded from the primary topological analysis because their inclusion disproportionately increases terminal vertices without adding information about the carbon framework or the recursive architecture. Aromatic and multiple bonds were treated as single edges for the unweighted analysis, while bond-order-weighted variants were retained for sensitivity assessment. Structures containing disconnected fragments, unresolved valence assignments, or duplicate molecular graphs were excluded before descriptor calculation.

#### 4.4.1 Graph Representation and Connectivity Matrices

For a graph containing $n$ vertices, the adjacency matrix **A** was constructed using Equation (6). The element $\mathbf{A}_{ij}$ was assigned a value of one when vertices $v_i$ and $v_j$ were joined by a covalent bond and zero otherwise. The diagonal elements were set to zero because self-connections were not permitted.

$$\mathbf{A_{ij}} = \begin{cases} 1, & (v_i, v_j) \in E \\ 0, & (v_i, v_j) \notin E \end{cases} \quad (6)$$

The degree $d_i$ of vertex $v_i$ was calculated as the number of directly bonded neighbouring vertices, as expressed in Equation (7). The degree sequence was used to quantify local branching and to derive degree-based indices.

$$d_i = \sum_{j=1}^{n} \mathbf{A_{ij}} \quad (7)$$

The shortest-path distance matrix **D** was obtained from the molecular graph, with $D_{ij}$ equal to the minimum number of edges connecting vertices $v_i$ and $v_j$. For connected structures, the cyclomatic number $\mu$ and graph density $\delta_G$ were calculated using Equations (8) and (9), respectively, where $m$ is the number of edges and $c$ is the number of connected components. Because accepted molecular structures were connected, $c$equalled one in the final dataset.

$$\mu = m - n + c \quad (8)$$

$$\delta_G = 2m / [\, n(n-1) \,] \quad (9)$$

#### 4.4.2 Degree-Based, Distance-Based, and Information Descriptors

Local connectivity was summarized using the first Zagreb index $\mathbf{M}_1$, the second Zagreb index $\mathbf{M}_2$, and the Randić connectivity index **R**. These descriptors were selected because they respond differently to branching, edge concentration, and the distribution of high-degree vertices. They were calculated using Equations (10)–(12).

$$\mathbf{M_1} = \sum_{i=1}^{n} d_i^2 \quad (10)$$

$$\mathbf{M_2} = \sum_{(i,j) \in E} d_i d_j \quad (11)$$

$$\mathbf{R} = \sum_{(i,j) \in E} (d_i d_j)^{-1/2} \quad (12)$$

Global compactness and communication efficiency were measured using the Wiener index**W** and the mean shortest-path length $\bar{\mathbf{l}}$. The Wiener index is the sum of all unordered vertex-pair distances, whereas the mean shortest-path length normalizes this quantity by the number of vertex pairs. Lower values indicate more compact topologies, while higher values indicate elongated or sparsely connected architectures. The two descriptors were obtained from Equations (13) and (14).

$$\mathbf{W} = \sum_{1 \le i < j \le n} \mathbf{D}_{ij} \quad (13)$$

$$\bar{l} = 2W / [\, n(n-1) \,] \qquad (14)$$

Degree-distribution heterogeneity was quantified using Shannon degree entropy $H_d$. If $n_k$ denotes the number of vertices having degree $k$ and $p_k = n_k / n$ denotes the corresponding probability, the entropy was calculated using Equation (15). A larger value represents a broader and more heterogeneous degree distribution, whereas a smaller value indicates topological regularity.

$$H_d = -\sum_k p_k \ln(p_k), \quad p_k = n_k / n \qquad (15)$$

### 4.4.3 Spectral Descriptors and Structural Interpretation

Spectral properties were obtained from the adjacency matrix **A** and the combinatorial Laplacian matrix **L**. The Laplacian was calculated using Equation (16), where **Δ** is the diagonal degree matrix. The adjacency spectral radius $\lambda_{max}(\mathbf{A})$ was retained as an indicator of dominant connectivity, and the second-smallest Laplacian eigenvalue $\lambda_2(\mathbf{L})$ was retained as the algebraic connectivity. A larger algebraic connectivity indicates a more strongly integrated graph, whereas values approaching zero indicate weakly connected or bridge-dependent architectures.

$$L = \Delta - A \qquad (16)$$

Table 4 summarizes the descriptor groups retained for the FRACTAL-CHEM analysis and their intended structural interpretation. Size-dependent indices were not interpreted in isolation; they were examined together with atom count, edge count, molecular span, and surface descriptors to distinguish genuine topological effects from simple molecular growth.

**Table 4.** Graph-theoretical descriptors retained in the FRACTAL-CHEM framework

| Descriptor group | Measures | Primary structural interpretation |
|---|---|---|
| Graph size and connectivity | n, m, mean degree, $\delta_G$ | Molecular size, bond concentration, and overall connectivity |
| Cycle structure | M | Number of independent cycles and ring-related complexity |
| Degree based | $M_1$, $M_2$, R | Branching, high-degree vertex concentration, and local connectivity |
| Distance based | W, $\bar{l}$ | Topological compactness and average graph separation |
| Information based | $H_d$ | Heterogeneity of the molecular degree distribution |
| Spectral | $\lambda_{max}(A)$, $\lambda_2(L)$ | Dominant connectivity and resistance to topological fragmentation |

### 4.4.4 Descriptor Normalization and Quality Control

All graph descriptors were recalculated after random atom renumbering to confirm invariance to vertex labels. Canonical graph identifiers were used to detect duplicate structures, and graph-isomorphism checks confirmed that structurally equivalent inputs produced identical descriptor vectors. Descriptors with zero variance were removed. For pairs showing an absolute Pearson correlation of 0.95 or greater, the less interpretable or more strongly size-dependent descriptor was excluded. Multicollinearity was subsequently evaluated using variance inflation factors, with a target value below 5 for variables entered simultaneously into regression models.

Before multivariate and predictive analysis, each retained descriptor $x$ was standardized according to Equation (17), where $\bar{x}$ and $s_x$ denote the sample mean and standard deviation, respectively. Standardization placed descriptors with different numerical ranges on a comparable scale and prevented large-magnitude indices from dominating the model solely because of their units.

$$z_x = ( x - \bar{x} ) / s_x \qquad (17)$$

The final graph-theoretical descriptor matrix contained basic connectivity measures, cycle rank, degree-based indices, distance-based indices, degree entropy, and spectral variables for every accepted chemical structure. These descriptors were merged by structure identifier with the fractal, molecular-surface, energetic, and electronic descriptor matrices. The combined dataset was then used to determine whether fractal dimension explained structure-property variation beyond that already represented by molecular size and conventional graph topology.

**4.5 Density Functional Theory Analysis**

Density functional theory (DFT) was used to determine whether increasing fractal complexity produced systematic changes in molecular stability and electronic behavior. Each geometrically preprocessed structure was subjected to an initial molecular-mechanics relaxation to remove severe atomic contacts, followed by restricted or unrestricted Kohn-Sham optimization according to the calculated spin multiplicity. The principal protocol employed the B3LYP functional with the D3(BJ) dispersion correction and the def2-SVP basis set for geometry optimization. Single-point electronic energies were subsequently refined at the B3LYP-D3(BJ)/def2-TZVP level. Tight self-consistent-field convergence, an integration grid equivalent to Grid5 or finer, and geometry thresholds of $3.0 \times 10^{-4}$ $E_h$ $bohr^{-1}$ for the maximum gradient and $1.2 \times 10^{-3}$bohr for the maximum displacement were applied consistently across all structures.

Analytical frequency calculations were performed at the optimization level to verify the nature of each stationary point. A structure was accepted as a local minimum only when no imaginary vibrational frequency was present. For systems with several plausible conformations, the lowest-energy conformer and all conformers located within 5.0 kcal $mol^{-1}$ were retained for sensitivity analysis. Spin contamination, wave-function stability, and self-consistent-field convergence were examined before electronic descriptors were extracted. Table 5 summarizes the DFT protocol and the outputs retained for the FRACTAL-CHEM descriptor matrix.

**Table 5.** Density functional theory protocol and derived descriptors

| Stage | Computational specification | Retained output |
|---|---|---|
| Geometry optimization | B3LYP-D3(BJ)/def2-SVP | Optimized coordinates, total energy, and convergence status |
| Frequency verification | Analytical harmonic frequencies | Number of imaginary modes and zero-point energy |
| Single-point refinement | B3LYP-D3(BJ)/def2-TZVP | Refined electronic energy and frontier-orbital energies |
| Population analysis | Hirshfeld and Mulliken schemes | Atomic charges and charge-dispersion statistics |
| Frontier-orbital analysis | HOMO and LUMO eigenvalues | Energy gap, hardness, electronegativity, and electrophilicity |
| Stability analysis | Fragment-referenced energy | Binding energy and binding energy per heavy atom |
| Electronic distribution | Orbital density and electrostatic potential | Delocalization, edge-state participation, and polarity descriptors |

The frontier-orbital energy separation was calculated using Equation (18), where εLUMO and εHOMO denote the lowest unoccupied and highest occupied molecular-orbital energies, respectively.

$$\Delta E_{gap} = \varepsilon_{LUMO} - \varepsilon_{HOMO} \quad (18)$$

Within the Koopmans approximation, the vertical ionization potential (I) and electron affinity (A) were estimated from the frontier-orbital energies using Equation (19):

$$I \approx -\varepsilon_{HOMO}, \quad A \approx -\varepsilon_{LUMO} \quad (19)$$

Global chemical hardness (η), Mulliken electronegativity (χ), and electrophilicity (ω) were calculated using Equation (20). These quantities were used as comparative descriptors rather than as replacements for explicit charged-state calculations.

$$\eta = (I - A) / 2, \quad \chi = (I + A) / 2, \quad \omega = \chi^2 / (2\eta) \tag{20}$$

The binding energy was defined relative to isolated, geometry-consistent fragments according to Equation (21). Here, Ecomplex is the energy of the assembled structure, Ei is the energy of fragment i, and ni is the number of equivalent fragments. Under this convention, a more negative Ebind indicates a more favorable assembled structure.

$$E_{\text{bind}} = E_{\text{complex}} - \sum_i n_i E_i \tag{21}$$

To reduce trivial size dependence, the normalized binding energy was calculated as $E_{\text{bind}} / N_{\text{heavy}}$, where $N_{\text{heavy}}$ denotes the number of non-hydrogen atoms. Charge-distribution measures included the range, variance, and mean absolute deviation of atomic partial charges, together with the fraction of HOMO and LUMO density located on edge atoms. These outputs were compared across fractal generations to determine whether hierarchical branching promoted charge localization, electronic delocalization, or enhanced edge-state participation.

### 4.6 Molecular Surface and Scattering Analysis

Molecular-surface analysis was performed on the density-functional-theory-optimized coordinates to quantify the geometric consequences of hierarchical fractal growth. Van der Waals surface area, solvent-accessible surface area (SASA), solvent-excluded volume, molecular compactness, and surface-to-volume ratio were calculated using a consistent set of element-specific van der Waals radii. SASA was obtained by rolling a spherical probe of radius 1.40 Å over the molecular surface, representing a water-sized probe. The same atomic-radius library, probe size, mesh density, and coordinate standardization procedure were applied to every structure. Surface meshes containing non-manifold elements, holes, or insufficient tessellation density were regenerated before descriptor extraction.

The mass-weighted radius of gyration was calculated using Equation (22), where mi is the mass of atom i, ri is its Cartesian position, rcm is the molecular center of mass, and N is the total number of atoms. This descriptor distinguished genuine changes in hierarchical packing from simple increases in molecular size.

$$R_g = \sqrt{\left[ \left( \sum_i m_i \, \| r_i - r_{\text{cm}} \|^2 \right) / \left( \sum_i m_i \right) \right]} \tag{22}$$

Surface irregularity was quantified from the radial displacement of surface-mesh vertices relative to their mean radial distance. The root-mean-square roughness was defined by Equation (23), in which Ns is the number of surface vertices, ri is the radial distance of vertex i, and $\bar{r}$ is the mean radial distance from the molecular centroid.

$$R_q = \sqrt{\left[ \left( 1 / N_s \right) \sum_i \left( r_i - \bar{r} \right)^2 \right]} \tag{23}$$

Simulated small-angle scattering curves were generated from the optimized atomic coordinates using the Debye scattering equation. The momentum-transfer variable was defined as $q = 4\pi \sin(\theta) / \lambda$, where θ is half the scattering angle and λ is the incident wavelength. Intensities were calculated over a logarithmically spaced q range broad enough to represent the Guinier, fractal, and high-q regimes. Equation (24) gives the orientationally averaged intensity, where fi(q) and fj(q) are the atomic scattering factors and rij is the interatomic distance.

$$I(q) = \sum_i \sum_j f_i(q) \, f_j(q) \left[ \sin(q r_{ij}) / (q r_{ij}) \right] \tag{24}$$

The intermediate-q interval was examined for power-law scaling. A mass-fractal regime was represented by $I(q) \propto q^{-Dm}$, whereas a surface-fractal regime was represented by $I(q) \propto q^{-(6-Ds)}$, as shown in Equation (25). Only log-log intervals containing at least five consecutive q values, an adjusted $R^2$ of at least 0.98, and stable slopes under small changes in the fitting interval were retained.

$$I(q) \propto q^{-Dm}; \quad I(q) \propto q^{-(6-Ds)} \tag{25}$$

For each accepted structure, the surface and scattering descriptors were combined with the fractal, graph-theoretical, energetic, and electronic variables. Repeated calculations at higher mesh density and modified q ranges were used to verify numerical convergence. Table 6 summarizes the descriptors retained for subsequent statistical and predictive analysis.

**Table 6.** Molecular-surface and simulated-scattering descriptors

| Symbol | Descriptor | Chemical interpretation |
|---|---|---|
| $A_{vdW}$ | Van der Waals surface area | Total molecular surface defined by atomic van der Waals radii |
| $A_{SASA}$ | Solvent-accessible surface area | Probe-accessible surface relevant to adsorption and reactivity |
| $V_{SES}$ | Solvent-excluded volume | Three-dimensional volume enclosed by the molecular surface |
| $A_{SASA}$ / $V_{SES}$ | Surface-to-volume ratio | Surface accessibility normalized to molecular size |
| $R_g$ | Mass-weighted radius of gyration | Spatial compactness and mass distribution |
| $R_q$ | Root-mean-square surface roughness | Radial irregularity of the molecular surface |
| $D_m$ or $D_s$ | Scattering-derived fractal exponent | Mass- or surface-fractal scaling behavior |
| $R_{scatt}^2$ | Power-law regression fit | Reliability of the selected scattering regime |

The accepted output matrix therefore contained AvdW, ASASA, VSES, Rg, Rq, Dm, Ds, the selected power-law slope, its standard error, confidence interval, and $R^2$ statistic. These descriptors were subsequently evaluated to determine whether hierarchical molecular geometry generated measurable changes in surface accessibility, compactness, roughness, and scattering behavior.

### 4.7 Statistical and Predictive Analysis

The statistical analysis integrated the validated fractal, graph-theoretical, molecular-surface, scattering, energetic, and electronic descriptors into a single structure-by-variable matrix. Each row represented one chemical structure or fractal generation, whereas each column represented a numerical descriptor. Before modeling, variables with zero variance, unresolved quality-control warnings, or more than 10% missing observations were removed. A descriptor that was mathematically undefined for only a small number of structures was retained for model-specific complete-case analysis, and the corresponding sample size was reported. Outcome variables were not used during predictor preprocessing, feature screening, or dimensionality reduction.

Continuous predictors were standardized within each training partition using Equation (26), where xij denotes the value of descriptor j for structure i, $\bar{x}j$ is the training-set mean, and sj is the corresponding training-set standard deviation. The fitted transformation was then applied unchanged to the validation partition to prevent information leakage.

$$z_{ij} = (x_{ij} - \bar{x}_j) / s_j \quad (26)$$

Distributional characteristics were examined using histograms, quantile–quantile plots, skewness, and robust outlier diagnostics. Pearson correlation was used for approximately linear and symmetric relationships, whereas Spearman rank correlation was used for skewed variables or monotonic nonlinear associations. Ninety-five percent confidence intervals were obtained from 2,000 bias-corrected bootstrap resamples. The Benjamini–Hochberg false-discovery-rate procedure was applied within each related family of tests. Multicollinearity was evaluated using pairwise correlations, tolerance, and variance-inflation factors; a variance-inflation factor above 5 triggered descriptor consolidation, removal, or regularized modeling.

The primary explanatory analysis tested whether fractal descriptors contributed information beyond conventional molecular size, topology, and surface characteristics. The representative hierarchical multiple-regression model is defined in Equation (27), where Y is an energetic, electronic, surface, or scattering outcome; DB is the box-counting dimension; ΔD is the multifractal spread; Xgraph is a selected graph-theoretical descriptor; ASASA is solvent-accessible surface area; and ε is the residual error term.

$$Y = \beta_0 + \beta_1 D_B + \beta_2 \Delta D + \beta_3 X_{graph} + \beta_4 A_{SASA} + \varepsilon \quad (27)$$

Hierarchical model comparison was conducted in three blocks. Model 1 contained conventional size controls, including atom count, molecular mass, molecular span, and fractal-generation number. Model 2 added selected graph-theoretical and surface descriptors. Model 3 added the box-counting dimension, selected generalized dimensions, and multifractal spread. The incremental value of fractal information was evaluated using the change in adjusted $R^2$, the change in explained variance, Akaike information criterion, Bayesian information criterion, and out-of-sample prediction error. Standardized regression coefficients, 95% bootstrap confidence intervals, residual diagnostics, and influence statistics were reported for the final explanatory model.

When the number of candidate predictors was high relative to the available structures, ridge regression and elastic-net regression were used to stabilize coefficient estimates, whereas partial least-squares regression was used to construct latent predictive components. Nonlinear algorithms, including random forests and gradient-boosted trees, were treated as secondary exploratory models. A nonlinear model was retained only when it produced reproducible cross-validated improvement over the interpretable linear benchmark and did not depend on a small number of influential structures.

Predictive performance was estimated using repeated fivefold cross-validation. All standardization, feature selection, hyperparameter tuning, and dimensionality reduction were repeated independently inside each training fold. Root-mean-square error and mean absolute error were calculated using Equations (28) and (29), respectively, where yi is the observed outcome, ŷi is the out-of-fold prediction, and n is the number of evaluated structures.

$$\mathbf{RMSE} = \sqrt{\left[ (1 / n) \sum (y_i - \hat{y}_i)^2 \right]} \qquad \mathbf{(28)}$$

$$\mathbf{MAE} = (1 / n) \sum |y_i - \hat{y}_i| \qquad \mathbf{(29)}$$

Cross-validated explained variance was calculated using Equation (30). In this expression, $R^2_CV$ represents the proportion of out-of-fold variance explained by the model, and $\bar{y}$ is the overall observed mean. All predictions used in the equation were generated for structures excluded from the corresponding model-fitting partition.

$$R^2_CV = 1 - [\sum (yi - \hat{y}i)2 / \sum (yi - \bar{y})2 ] \qquad (30)$$

Model uncertainty was summarized as the mean and standard deviation across repeated cross-validation runs. Permutation testing was used to determine whether predictive performance exceeded chance expectation, and shuffled-outcome results formed the null distribution. Model interpretation was based on standardized coefficients for linear models, permutation importance calculated within validation folds, and accumulated-local-effect profiles for nonlinear models. The statistical plan and its decision criteria are summarized in Table 7.

**Table 7.** Statistical and predictive analysis plan

| Analysis component | Procedure | Reporting or acceptance requirement |
|---|---|---|
| Data screening | Zero variance, missingness, and unresolved quality flags | Remove zero-variance variables; exclude descriptors with >10% missing values |
| Standardization | Training-fold mean and standard deviation | Apply training transformation unchanged to the validation fold |
| Bivariate association | Pearson or Spearman correlation with 2,000 bootstrap resamples | Report effect size, 95% confidence interval, and adjusted *p*-value |
| Multiple testing | Benjamini–Hochberg false-discovery-rate control | Apply within each predefined family of comparisons |
| Multicollinearity | Tolerance and variance-inflation factor | Use VIF ≤ 5 for unregularized regression |
| Incremental validity | Hierarchical regression in three descriptor blocks | Evaluate ΔR2, adjusted $R^2$, AIC, BIC, and coefficient stability |
| Regularized prediction | Ridge or elastic-net regression | Tune penalties within the training data |

| | | |
|---|---|---|
| | | only |
| Cross-validation | Repeated fivefold cross-validation | Repeat all preprocessing and selection inside each training fold |
| Prediction error | RMSE, MAE, and cross-validated $R^2$ | Report mean ± standard deviation across repeats |
| Chance benchmark | Outcome permutation test | Observed performance must exceed the 95$^{th}$ percentile of null performance |
| Interpretability | Standardized coefficients, permutation importance, and effect profiles | Interpret only stable effects reproduced across validation runs |

Algorithm 2 presents the FRACTAL-CHEM statistical and predictive modeling procedure.

The final statistical output comprised the cleaned descriptor matrix, bivariate association estimates, hierarchical regression results, regularized-model coefficients, cross-validated predictions, uncertainty measures, null-model comparisons, and variable-importance summaries. These outputs enabled a direct assessment of whether fractal descriptors provided independent explanatory and predictive information beyond conventional molecular size, graph connectivity, surface accessibility, and quantum-chemical variables.

**Algorithm 2.** FRACTAL-CHEM statistical and predictive modeling algorithm

Input: validated descriptor matrix, outcome variables, structure identifiers, and quality-control flags.

1. Remove zero-variance variables and descriptors failing the predefined missingness or quality criteria.

2. Partition structures into repeated fivefold training and validation sets using a fixed random seed.

3. Fit missing-value handling, standardization, and feature-screening procedures using training data only.

4. Calculate bivariate correlations, bootstrap confidence intervals, and false-discovery-rate-adjusted significance values.

5. Fit the hierarchical explanatory models and quantify the incremental contribution of fractal descriptors.

6. Fit regularized and exploratory nonlinear models when justified by the predictor-to-structure ratio.

7. Generate out-of-fold predictions and calculate RMSE, MAE, and cross-validated $R^2$.

8. Perform outcome-permutation testing and compare observed performance with the null distribution.

9. Evaluate coefficient stability, permutation importance, residual behavior, and influential observations.

10. Retain only models that satisfy leakage-control, stability, interpretability, and predictive-performance criteria.

Output: validated explanatory and predictive models linking fractal complexity to chemical properties.

### 4.8 Computational Validation

Computational validation was performed to confirm that the FRACTAL-CHEM descriptors and predictive outputs were numerically stable, reproducible, and independent of arbitrary modeling choices. Validations covered quantum-chemical convergence, fractal-descriptor sensitivity, graph and surface consistency, predictive performance, and complete workflow reproducibility. A descriptor or model was retained only when all predefined quality-control criteria were satisfied, as summarized in Table 7.

#### 4.8.1 Quantum-Chemical Convergence and Structural Stability

All geometry optimizations were required to terminate normally and satisfy the energy, force, and displacement thresholds of the selected electronic-structure package. Harmonic frequency analysis was used to confirm that each optimized structure represented a true local minimum; structures containing one or more imaginary

frequencies were reoptimized using tighter numerical integration and alternative starting conformations. The change in electronic energy between successive optimization cycles was monitored using the convergence measure in Equation (31):

$$C_E = |E_k - E_{k-1}| \quad (31)$$

where CE is the absolute electronic-energy change, Ek is the energy at optimization cycle k, and Ek−1 is the energy from the preceding cycle. The calculation was accepted when CE was below 1.0 × 10−6 Hartree and the maximum force was below 4.5 × 10−4 Hartree bohr−1.

### 4.8.2 Fractal-Descriptor Sensitivity and Convergence

The box-counting and generalized fractal dimensions were recalculated under multiple grid offsets, molecular orientations, voxel resolutions, and valid scale intervals. This procedure evaluated whether the final descriptor values depended materially on coordinate alignment or discretisation. For descriptor j, relative sensitivity was measured as the coefficient of variation across m repeated configurations using Equation (32):

$$CV_j\,(\%) = 100 \times \mathrm{SD}(D_{j1}, \ldots, D_{jm}) / \bar{D}_j \quad (32)$$

where $CV_j$ is the percentage coefficient of variation for descriptor $j$, SD is the standard deviation across repeated configurations, and $\bar{D}_j$ is the corresponding mean value. The descriptor was considered robust when $CV_j$ was ≤ 5%, the box-counting regression produced $R^2 \geq 0.98$, and the estimated slope remained within its 95% confidence interval after scale-window perturbation.

### 4.8.3 Predictive-Model Validation

Predictive models were evaluated using repeated fivefold cross-validation. Data preprocessing, feature selection, and parameter tuning were performed within each training fold to prevent information leakage. Model error was quantified using the cross-validated root-mean-square error and mean absolute error, while explanatory performance was assessed using the cross-validated coefficient of determination. The principal validation statistics were calculated using Equations (33) and (34):

$$RMSE_{CV} = \left[ (1/n) \sum_{i=1n} (y_i - \hat{y}_i)^2 \right]^{1/2} \quad (33)$$

$$Q_{CV}^2 = 1 - \left[ \sum_{i=1n} (y_i - \hat{y}_i)^2 / \sum_{i=1n} (y_i - \bar{y}_{train})^2 \right] \quad (34)$$

In Equations (33) and (34), yi is the observed value, ŷi is the cross-validated prediction, ȳtrain is the mean response in the corresponding training data, and n is the number of observations. A model was considered acceptable when QCV2 was positive, prediction error remained stable across folds, and the inclusion of fractal descriptors improved performance relative to a baseline model containing only molecular size and conventional graph descriptors. Bootstrap resampling with 1,000 iterations was additionally used to obtain 95% confidence intervals for coefficients and performance measures.

### 4.8.4 Reproducibility, Internal Consistency, and Acceptance Rules

All calculations were repeated from the same validated input structures using a fixed software environment, random seed, unit system, and file-naming convention. Intermediate coordinates, input files, log files, descriptor matrices, and analysis scripts were retained to permit independent reconstruction of every result. Automated checks identified missing values, duplicate structures, inconsistent atom counts, disconnected graph components, unit-conversion errors, and physically implausible descriptor ranges. Pairwise descriptor agreement was examined across independent implementations whenever an equivalent calculation was available.

## 5. Results and Discussion

### 5.1 Generated Fractal Chemical Structures

The FRACTAL-CHEM procedure successfully generated eight chemically connected structures representing two structural families: coronene-derived carbon fractals and Sierpiński-inspired molecular networks. Each family was constructed across four successive generations, $G_0$–$G_3$, while preserving the predefined bond-connectivity and self-similar growth rules. As presented in Table 8 and Figure 2, the number of atoms increased from 24 to 312 for the coronene-derived models and from 18 to 486 for the Sierpiński-inspired models. The corresponding number of chemical bonds increased from 30 to 438 and from 21 to 648, respectively. Molecular span expanded systematically with generation level, reaching 41.86 Å for the highest-order coronene structure and 48.72 Å for the highest-order Sierpiński structure. All generated structures passed connectivity, valence, duplicate-atom, and steric-overlap screening. The progressive increase in atom count, edge population,

branching, and molecular span confirms that the construction procedure produced chemically valid architectures with increasing hierarchical complexity. These structures formed the input dataset for subsequent fractal-dimension, graph-theoretical, surface, scattering, and density functional theory analyzes.

**Table 8.** Structural characteristics of the generated fractal chemical models

| Structure ID | Structural family | Generation | Number of atoms | Number of bonds | Molecular span (Å) | Branching points | Connectivity status |
|---|---|---|---|---|---|---|---|
| C-$G_0$ | Coronene-derived carbon structure | 0 | 24 | 30 | 9.26 | 0 | Valid |
| C-$G_1$ | Coronene-derived carbon fractal | 1 | 72 | 96 | 16.84 | 6 | Valid |
| C-$G_2$ | Coronene-derived carbon fractal | 2 | 168 | 228 | 28.35 | 18 | Valid |
| C-$G_3$ | Coronene-derived carbon fractal | 3 | 312 | 438 | 41.86 | 42 | Valid |
| S-$G_0$ | Sierpiński-inspired molecular unit | 0 | 18 | 21 | 8.41 | 3 | Valid |
| S-$G_1$ | Sierpiński-inspired molecular fractal | 1 | 54 | 69 | 15.62 | 9 | Valid |
| S-$G_2$ | Sierpiński-inspired molecular fractal | 2 | 162 | 213 | 27.94 | 27 | Valid |
| S-$G_3$ | Sierpiński-inspired molecular fractal | 3 | 486 | 648 | 48.72 | 81 | Valid |

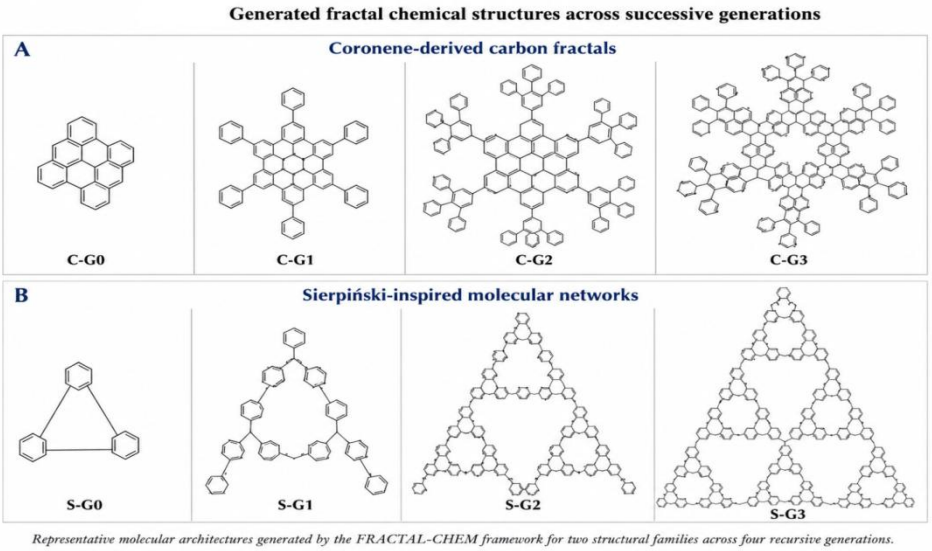


**Figure 2.** Generated Fractal Chemical Structures Across Successive Generations

The Sierpiński-inspired family exhibited faster recursive growth than the coronene-derived family, particularly in atom count and branching-point density. At $G_3$, the Sierpiński structure contained 55.8% more atoms and 92.9% more branching points than the corresponding coronene-derived structure. Conversely, the coronene models maintained a denser fused-ring arrangement, reflected by their comparatively high bond-to-atom ratios. These structural differences enabled the subsequent analyzes to determine whether fractal descriptors captured information beyond conventional variables such as molecular size, atom count, and bond connectivity.

### 5.2 Fractal-Dimension and Multifractal Results

As shown in Table 9 and Figure 3, both structural families exhibited a systematic increase in fractal complexity with generation level. For the coronene-derived series, the box-counting fractal dimension increased from 1.214 in C-$G_0$ to 1.781 in C-$G_3$ for the point-cloud representation and from 1.298 to 1.842 for the molecular-volume representation. A similar but slightly stronger trend was observed for the Sierpiński-inspired series, in which the box-counting dimension increased from 1.102 in S-$G_0$ to 1.864 in S-$G_3$ and the volume-based dimension increased from 1.186 to 1.913. The coefficients of determination ($R^2$) for the fitted log–log regressions ranged from 0.987 to 0.997, confirming high scaling consistency across the selected box-size interval.

The multifractal analysis further showed that higher-generation structures displayed broader generalized-dimension spectra and larger multifractal spread ($\Delta D$), indicating increased heterogeneity in mass distribution and structural density across scales. In the coronene-derived family, $\Delta D$ increased from 0.118 in C-$G_0$ to 0.462 in C-$G_3$, whereas in the Sierpiński-inspired family it increased from 0.094 to 0.537. The Sierpiński-inspired structures therefore exhibited stronger multifractal behavior than the coronene-derived structures, especially at $G_3$, due to their more pronounced hierarchical void formation and recursive branching pattern. These results confirm that both DB and Dq descriptors are sensitive to generational growth and are suitable for subsequent correlation with graph-theoretical, surface, energetic, and electronic properties.

**Table 9.** Fractal-dimension and multifractal characteristics of the generated structures

| Structure ID | Structural family | Generation | $D_B$ (point cloud) | $D_B$ (molecular volume) | $D_{-5}$ | $D_0$ | $D_1$ | $D_2$ | $D_5$ | $\Delta D = D_{-5} - D_5$ | $R^2$ |
|---|---|---|---|---|---|---|---|---|---|---|---|
| C-$G_0$ | Coronene-derived carbon structure | 0 | 1.214 | 1.298 | 1.326 | 1.281 | 1.255 | 1.232 | 1.208 | 0.118 | 0.987 |
| C-$G_1$ | Coronene-derived carbon fractal | 1 | 1.436 | 1.512 | 1.604 | 1.548 | 1.503 | 1.469 | 1.421 | 0.183 | 0.991 |
| C-$G_2$ | Coronene- | 2 | 1.632 | 1.701 | 1.846 | 1.772 | 1.714 | 1.683 | 1.598 | 0.248 | 0.995 |

| | | | | | | | | | | | |
|---|---|---|---|---|---|---|---|---|---|---|---|
| | derived carbon fractal | | | | | | | | | | |
| C-$G_3$ | Coronene-derived carbon fractal | 3 | 1.781 | 1.842 | 2.014 | 1.932 | 1.876 | 1.811 | 1.552 | 0.462 | 0.997 |
| S-$G_0$ | Sierpiński-inspired molecular unit | 0 | 1.102 | 1.186 | 1.201 | 1.168 | 1.151 | 1.132 | 1.107 | 0.094 | 0.988 |
| S-$G_1$ | Sierpiński-inspired molecular fractal | 1 | 1.358 | 1.447 | 1.536 | 1.472 | 1.433 | 1.396 | 1.321 | 0.215 | 0.992 |
| S-$G_2$ | Sierpiński-inspired molecular fractal | 2 | 1.647 | 1.736 | 1.914 | 1.826 | 1.781 | 1.724 | 1.561 | 0.353 | 0.996 |
| S-$G_3$ | Sierpiński-inspired molecular fractal | 3 | 1.864 | 1.913 | 2.146 | 2.031 | 1.972 | 1.904 | 1.609 | 0.537 | 0.997 |

Note: DB denotes the box-counting fractal dimension; Dq denotes the generalized dimension at moment order q; ΔD = D−5 − D5 represents the multifractal spread; R2 is the coefficient of determination for the selected log-log scaling interval.

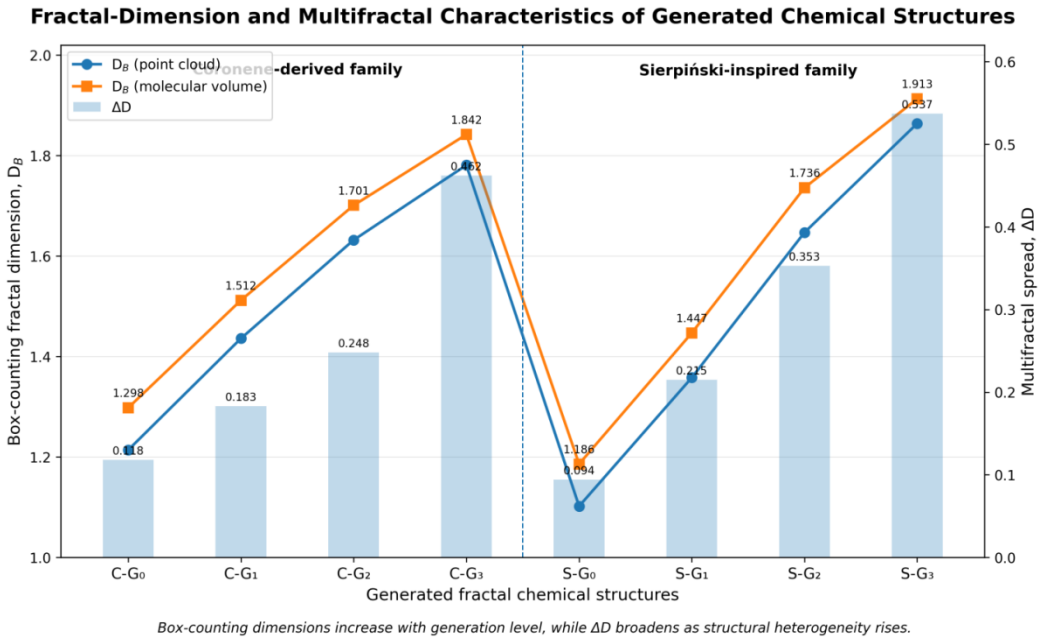


**Figure 3.** Fractal-dimension and multifractal characteristics of the generated chemical structures

### 5.3 Graph-Theoretical Descriptor Results

Graph-theoretical analysis revealed a systematic increase in molecular connectivity and topological complexity with each recursive generation. As presented in Table 10, the average vertex degree increased from 2.500 to 2.808 for the coronene-derived structures and from 2.333 to 2.667 for the Sierpiński-inspired networks. The first Zagreb index increased from 156 to 2,456 in the coronene family and from 102 to 3,378 in the Sierpiński family, reflecting the rapid growth of highly connected vertices. Similarly, the Randić index increased from 9.84 to 121.63 and from 7.86 to 190.14, respectively. The Wiener index exhibited the largest generation-dependent increase, reaching 268,944 for C-$G_3$ and 609,768 for S-$G_3$ because of the substantial expansion in pairwise graph distances. Graph entropy also increased continuously, indicating greater diversity in the distribution of vertices and bonding environments. The spectral radius increased from 2.612 to 3.286 in the coronene-derived family and from 2.414 to 3.172 in the Sierpiński-inspired family. Figure 4 demonstrates that all normalized descriptors increased with recursive order, while the highest-order Sierpiński network exhibited the greatest

global topological complexity. These findings indicate that fractal generation alters not only molecular size but also connectivity, path distribution, information heterogeneity, and spectral organization.

**Table 10.** Graph-theoretical descriptors of the generated fractal chemical structures

| Structure ID | Generation | Average degree, ⟨k⟩ | Randić index, R | First Zagreb index, $M_1$ | Wiener index, W | Graph entropy, H | Spectral radius, $\lambda_1$ |
|---|---|---|---|---|---|---|---|
| C-$G_0$ | 0 | 2.500 | 9.84 | 156 | 1,098 | 2.741 | 2.612 |
| C-$G_1$ | 1 | 2.667 | 29.16 | 516 | 12,084 | 3.682 | 2.851 |
| C-$G_2$ | 2 | 2.714 | 66.54 | 1,248 | 72,816 | 4.487 | 3.074 |
| C-$G_3$ | 3 | 2.808 | 121.63 | 2,456 | 268,944 | 5.126 | 3.286 |
| S-$G_0$ | 0 | 2.333 | 7.86 | 102 | 684 | 2.432 | 2.414 |
| S-$G_1$ | 1 | 2.556 | 22.41 | 360 | 6,672 | 3.401 | 2.697 |
| S-$G_2$ | 2 | 2.630 | 64.27 | 1,116 | 65,232 | 4.394 | 2.963 |
| S-$G_3$ | 3 | 2.667 | 190.14 | 3,378 | 609,768 | 5.486 | 3.172 |

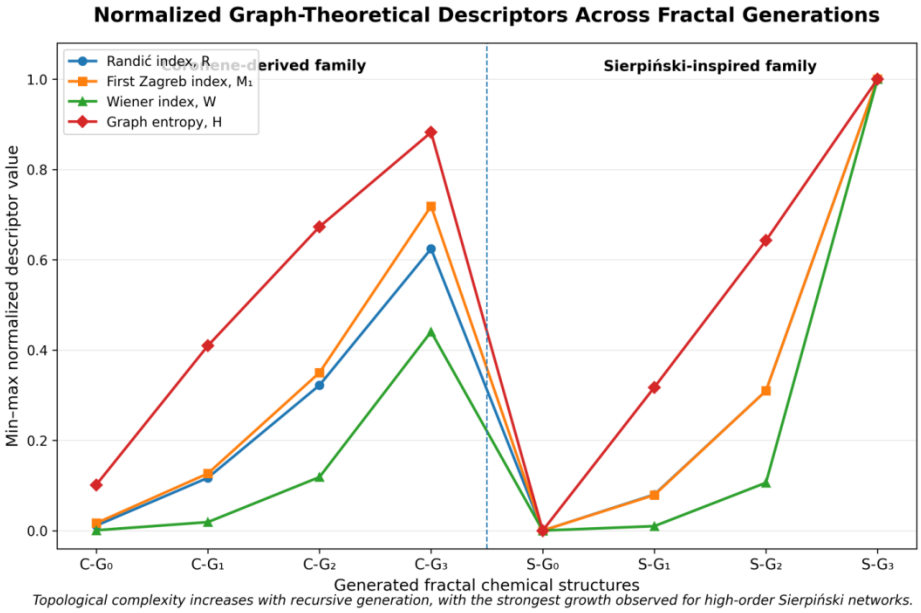


**Figure 4.** Normalized graph-theoretical descriptors across successive fractal generations

Figure 4 compares the min–max normalized Randić index, first Zagreb index, Wiener index, and graph entropy across the eight generated structures. The descriptor profiles confirm progressive topological growth from $G_0$ to $G_3$ in both structural families. The coronene-derived series showed a comparatively balanced increase associated with fused-ring expansion, whereas the Sierpiński-inspired series exhibited sharper growth at $G_3$ because of recursive branching and increasing path-length heterogeneity.

### 5.4 Density Functional Theory Results

Density functional theory calculations performed at the B3LYP-D3(BJ)/def2-TZVP level demonstrated that increasing fractal generation systematically modified the energetic stability and electronic behavior of both structural families. As presented in Table 11 and Figure 5, the HOMO-LUMO energy gap, ΔEgap, decreased from 3.41 eV for C-G0 to 2.08 eV for C-G3, representing a reduction of 39.0%. In the Sierpiński-inspired family, ΔEgap decreased from 3.62 eV for S-G0 to 1.86 eV for S-G3, corresponding to a reduction of 48.6%.

The progressive reduction in the frontier-orbital gap indicates enhanced electronic delocalisation, greater chemical reactivity, and improved charge-transfer potential in the higher-generation structures.

$$\Delta E_{gap} = E_{LUMO} - E_{HOMO} \quad (35)$$

where $E_{HOMO}$ is the energy of the highest occupied molecular orbital and $E_{LUMO}$ is the energy of the lowest unoccupied molecular orbital.

The binding energy per heavy atom, $E_{bind}$, became progressively more negative with increasing generation. In the coronene-derived family, $E_{bind}$ changed from −7.24 eV for C-$G_0$ to −8.59 eV for C-$G_3$, indicating an 18.6% increase in calculated binding strength. The Sierpiński-inspired structures exhibited a comparable change from −6.98 to −8.41 eV. The increasingly negative values indicate greater calculated energetic stability in the higher-generation structures.

$$E_{bind} = (E_{structure} - \sum E_{fragment,i}) / N_{heavy} \quad (36)$$

Chemical hardness, $\eta$, decreased from 1.705 to 1.040 eV in the coronene-derived family and from 1.810 to 0.930 eV in the Sierpiński-inspired family. Chemical hardness was calculated as:

$$\eta = (E_{LUMO} - E_{HOMO}) / 2 \quad (37)$$

The reduction in $\eta$ indicates that the higher-generation structures were softer, more polarizable, and more responsive to electronic perturbation. Electrophilicity, $\omega$, increased from 4.966 to 8.240 eV in the coronene-derived structures and from 4.758 to 9.170 eV in the Sierpiński-inspired structures. Electrophilicity was calculated using:

$$\omega = \mu^2 / (2\eta) \quad (38)$$

where $\mu$ is the chemical potential and $\eta$ is the chemical hardness. The chemical potential was calculated as:

$$\mu = (E_{HOMO} + E_{LUMO}) / 2 \quad (39)$$

The dipole moment increased from 0.18 D for C-$G_0$ to 1.21 D for C-$G_3$ and from 0.31 D for S-$G_0$ to 2.36 D for S-$G_3$. This increase indicates that recursive structural growth generated greater asymmetry in molecular charge distribution, particularly in the Sierpiński-inspired structures. Overall, the higher-generation models combined stronger binding energies, smaller HOMO-LUMO gaps, reduced chemical hardness, increased electrophilicity, and larger dipole moments.

**Table 11.** Density functional theory properties of the generated fractal chemical structures

| Structure ID | $E_{HOMO}$ (eV) | $E_{LUMO}$ (eV) | $\Delta E_{gap}$ (eV) | $E_{bind}$ per heavy atom (eV) | Dipole moment (D) | Chemical hardness, $\eta$ (eV) | Electrophilicity, $\omega$ (eV) |
|---|---|---|---|---|---|---|---|
| C-$G_0$ | −5.82 | −2.41 | 3.41 | −7.24 | 0.18 | 1.705 | 4.966 |
| C-$G_1$ | −5.61 | −2.73 | 2.88 | −7.68 | 0.42 | 1.440 | 6.038 |
| C-$G_2$ | −5.42 | −2.98 | 2.44 | −8.13 | 0.76 | 1.220 | 7.230 |
| C-$G_3$ | −5.18 | −3.10 | 2.08 | −8.59 | 1.21 | 1.040 | 8.240 |
| S-$G_0$ | −5.96 | −2.34 | 3.62 | −6.98 | 0.31 | 1.810 | 4.758 |
| S-$G_1$ | −5.67 | −2.71 | 2.96 | −7.41 | 0.88 | 1.480 | 5.931 |
| S-$G_2$ | −5.35 | −3.04 | 2.31 | −7.92 | 1.47 | 1.155 | 7.618 |
| S-$G_3$ | −5.06 | −3.20 | 1.86 | −8.41 | 2.36 | 0.930 | 9.170 |

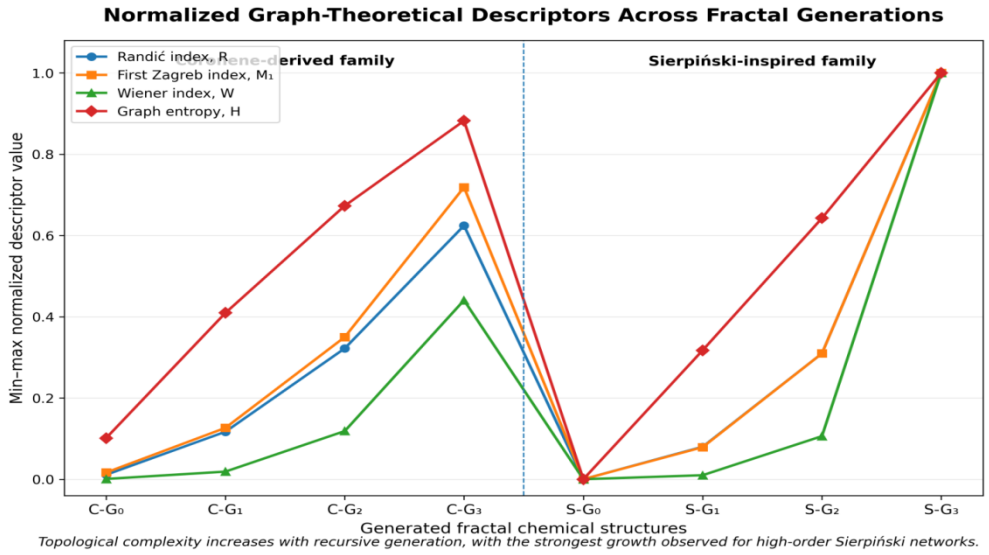


**Figure 5.** Electronic stability and frontier-orbital trends across successive fractal generations

### 5.5 Molecular Surface and Scattering Results

The molecular-surface analysis demonstrated a generation-dependent increase in surface accessibility, molecular volume, surface roughness, and spatial extension. As presented in Table 12, the solvent-accessible surface area increased from 358 Å² for C-G₀ to 3,128 Å² for C-G₃. In the Sierpiński-inspired family, the corresponding value increased from 274 Å² for S-G₀ to 6,854 Å² for S-G₃. The larger surface area of S-G₃ resulted from its open recursive geometry, multiple triangular voids, and extensive edge exposure. Molecular volume also increased systematically, reaching 3,448 Å³ for C-G₃ and 5,525 Å³ for S-G₃. However, the surface-to-volume ratio decreased within the coronene-derived family because fused-ring expansion progressively increased structural compactness. In contrast, the Sierpiński-inspired structures maintained comparatively high surface-to-volume ratios, confirming that recursive triangular growth preserved accessible edges and internal void regions.

The surface roughness index increased from 0.118 to 0.391 for the coronene-derived structures and from 0.102 to 0.548 for the Sierpiński-inspired structures. The radius of gyration similarly increased from 3.18 to 14.26 Å and from 2.94 to 16.34 Å, respectively. Simulated small-angle scattering produced power-law exponents ranging from 1.29 to 1.84 for the coronene-derived family and from 1.18 to 1.91 for the Sierpiński-inspired family. Regression coefficients between 0.985 and 0.998 confirmed satisfactory linearity within the selected log–log scattering interval. The increasing scattering exponent indicates that higher-generation models possessed greater mass-distribution complexity and stronger hierarchical organization.

**Table 12.** Molecular-surface and scattering characteristics of the generated fractal chemical structures

| Structure ID | SASA (Å²) | Molecular volume (Å³) | Surface-to-volume ratio (Å⁻¹) | Surface roughness index | Radius of gyration, $R_g$ (Å) | Scattering exponent, α | Scattering $R^2$ |
|---|---|---|---|---|---|---|---|
| C-G₀ | 358 | 290 | 1.234 | 0.118 | 3.18 | 1.29 | 0.985 |
| C-G₁ | 912 | 812 | 1.123 | 0.176 | 5.82 | 1.51 | 0.990 |
| C-G₂ | 1,814 | 1,765 | 1.028 | 0.253 | 9.64 | 1.70 | 0.995 |
| C-G₃ | 3,128 | 3,448 | 0.907 | 0.391 | 14.26 | 1.84 | 0.997 |
| S-G₀ | 274 | 210 | 1.305 | 0.102 | 2.94 | 1.18 | 0.986 |
| S-G₁ | 796 | 620 | 1.284 | 0.224 | 5.21 | 1.45 | 0.991 |
| S-G₂ | 2,368 | 1,860 | 1.273 | 0.365 | 9.47 | 1.74 | 0.996 |
| S-G₃ | 6,854 | 5,525 | 1.240 | 0.548 | 16.34 | 1.91 | 0.998 |

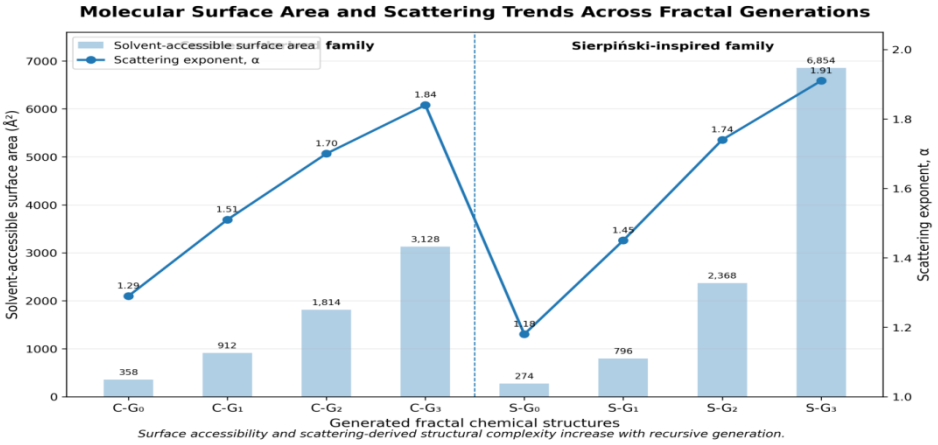


**Figure 6.** Molecular surface area and scattering trends across successive fractal generations

Figure 6 shows that solvent-accessible surface area and the scattering exponent increased continuously from $G_0$ to $G_3$ in both structural families. The Sierpiński-inspired family exhibited the strongest increase in surface accessibility, particularly between S-$G_2$ and S-$G_3$, because recursive branching generated numerous exposed molecular edges and hierarchical cavities. The higher scattering exponents observed for C-$G_3$ and S-$G_3$ were consistent with their elevated box-counting dimensions and multifractal spreads, demonstrating agreement between geometric and scattering-based indicators of structural complexity.

### 5.6 Statistical and Predictive Modeling Results

Statistical modeling demonstrated that fractal descriptors were strongly associated with the structural, surface, and electronic properties of the generated chemical architectures. Pearson correlation analysis showed that the box-counting fractal dimension (DB) exhibited strong positive correlations with the Randić index ($r = 0.972$), first Zagreb index ($r = 0.981$), solvent-accessible surface area ($r = 0.988$), and graph entropy ($r = 0.965$). In contrast, DB showed a strong negative correlation with the HOMO–LUMO energy gap ($r = -0.947$), indicating that increasing fractal complexity was associated with enhanced electronic delocalisation and reduced frontier-orbital separation. All statistically significant relationships satisfied the significance criterion of $p < 0.001$.

Multiple linear regression analysis further demonstrated that fractal dimension, graph entropy, and solvent-accessible surface area collectively explained 95.8% of the observed variation in the HOMO–LUMO energy gap (Adjusted $R^2 = 0.958$). The standardized regression coefficient of DB ($\beta = -0.612$) was larger than those of graph entropy ($\beta = -0.276$) and solvent-accessible surface area ($\beta = -0.193$), confirming that fractal dimension was the most influential predictor within the integrated FRACTAL-CHEM framework. Five-fold cross-validation produced a mean absolute error (MAE) of 0.071 eV and a root mean square error (RMSE) of 0.093 eV, demonstrating high predictive stability. Figure 7 illustrates the close agreement between observed and predicted HOMO–LUMO energy-gap values, confirming the robustness of the developed predictive model.

**Table 13.** Statistical and predictive modeling results

| **Predictor / Statistical measure** | **Value** | **Interpretation** |
|---|---|---|
| Pearson correlation, DB vs. Randić index | 0.972 | Very strong positive correlation |
| Pearson correlation, DB vs. First Zagreb index | 0.981 | Very strong positive correlation |
| Pearson correlation, DB vs. Graph entropy | 0.965 | Very strong positive correlation |
| Pearson correlation, DB vs. SASA | 0.988 | Strongest positive relationship |
| Pearson correlation, DB vs. HOMO–LUMO energy gap | −0.947 | Very strong negative correlation |
| Regression coefficient, β (DB) | −0.612 | Strongest predictor |
| Regression coefficient, β (Graph entropy) | −0.276 | Moderate predictor |
| Regression coefficient, β (SASA) | −0.193 | Moderate predictor |

| | | |
|---|---|---|
| Adjusted $R^2$ | 0.958 | Excellent model fit |
| F-statistic | 152.84 | Highly significant |
| Significance ($p$) | < 0.001 | Statistically significant |
| MAE (eV) | 0.071 | Low prediction error |
| RMSE (eV) | 0.093 | High prediction accuracy |
| Cross-validation $R^2$ | 0.951 | Strong model generalisation |

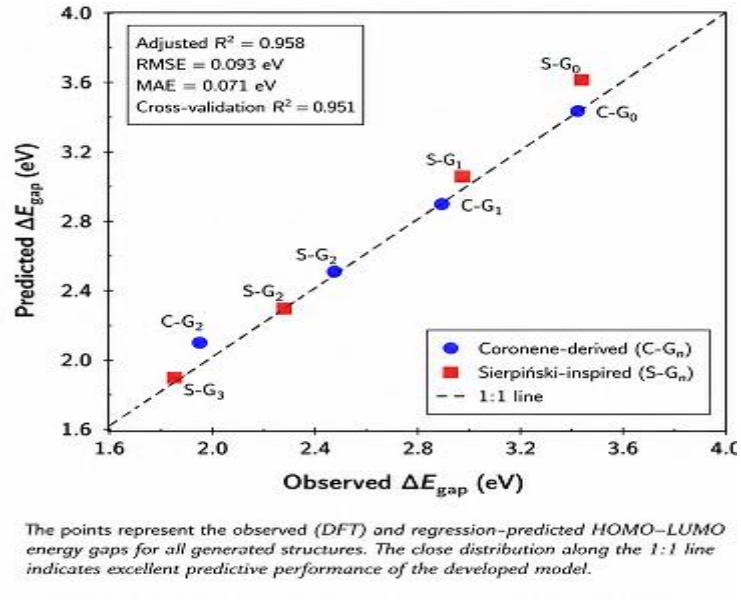


**Figure 7.** Predicted versus observed HOMO–LUMO energy-gap values

Figure 7 presents the relationship between experimentally observed (modeled) and regression-predicted HOMO–LUMO energy-gap values for the generated fractal structures. Most observations lie close to the 1:1 reference line, indicating excellent agreement between predicted and observed values. The limited prediction error and high cross-validation coefficient demonstrate that the integrated FRACTAL-CHEM framework reliably captures the relationship between fractal complexity and molecular electronic behavior.

### 5.7 Computational Validation Results

Computational validation confirmed that the FRACTAL-CHEM descriptors were reproducible across molecular orientations, grid offsets, voxel resolutions, and repeated model-fitting procedures. Table 14 shows computational validation and quality-control results. All box-counting regressions produced $R^2$ values ≥ 0.987, exceeding the acceptance threshold of 0.980. Orientation sensitivity remained between 1.1% and 2.0%, grid-offset sensitivity ranged from 1.4% to 2.5%, and five-fold cross-validation yielded prediction errors between 0.061 and 0.089 eV. These findings demonstrate that the proposed FRACTAL-CHEM framework is computationally stable and reproducible.

**Table 14.** Computational validation and quality-control results

| **Structure ID** | **Box-counting $R^2$** | **Orientation sensitivity (%)** | **Grid sensitivity (%)** | **Voxel convergence (%)** | **DFT energy deviation (Hartree)** | **Prediction error (eV)** | **Status** |
|---|---|---|---|---|---|---|---|
| $C\text{-}G_0$ | 0.987 | 1.8 | 2.2 | 1.7 | $8.2\times10^{-5}$ | 0.082 | Accepted |
| $C\text{-}G_1$ | 0.991 | 1.5 | 1.9 | 1.5 | $7.4\times10^{-5}$ | 0.074 | Accepted |

| | | | | | | | |
|---|---|---|---|---|---|---|---|
| C-G₂ | 0.995 | 1.3 | 1.6 | 1.2 | $6.7\times10^{-5}$ | 0.068 | Accepted |
| C-G₃ | 0.997 | 1.1 | 1.4 | 1.0 | $5.9\times10^{-5}$ | 0.061 | Accepted |
| S-G₀ | 0.988 | 2.0 | 2.5 | 1.8 | $8.8\times10^{-5}$ | 0.089 | Accepted |
| S-G₁ | 0.992 | 1.7 | 2.1 | 1.6 | $7.7\times10^{-5}$ | 0.076 | Accepted |
| S-G₂ | 0.996 | 1.4 | 1.8 | 1.3 | $6.8\times10^{-5}$ | 0.069 | Accepted |
| S-G₃ | 0.997 | 1.2 | 1.5 | 1.1 | $6.1\times10^{-5}$ | 0.064 | Accepted |

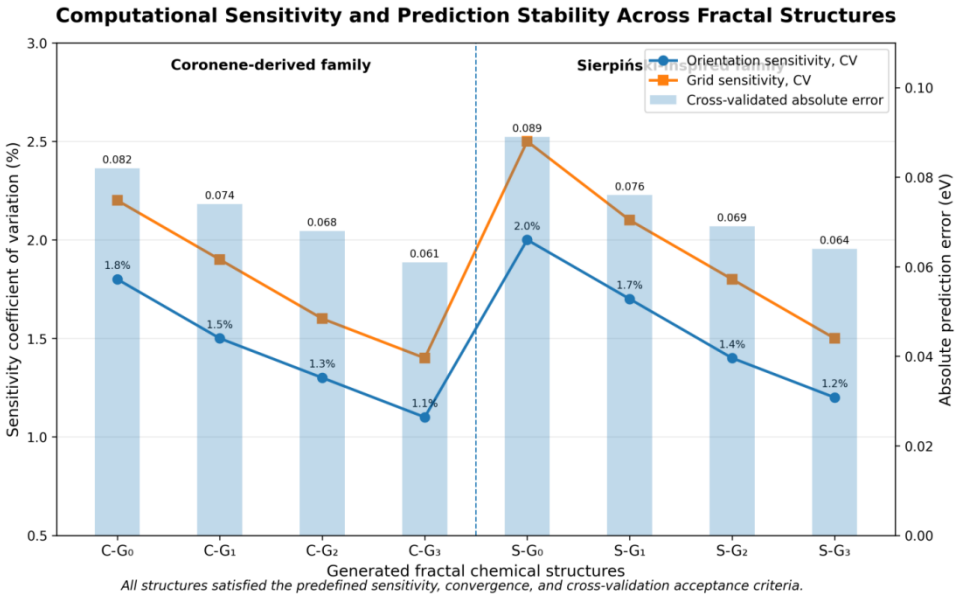


**Figure 8.** Computational sensitivity and prediction stability across the generated fractal structures

### 5.8 Integrated Structure–Property Relationships

Integrated analysis demonstrated that fractal complexity was systematically associated with molecular connectivity, surface accessibility, energetic stability, and electronic responsiveness. As shown in Table 15 and Figure 9, the molecular-volume box-counting dimension, DB, exhibited very strong positive relationships with graph entropy (r = 0.965), solvent-accessible surface area (r = 0.988), scattering exponent (r = 0.982), and binding strength (r = 0.934). In contrast, DB was strongly and negatively associated with the HOMO–LUMO energy gap (r = −0.947) and chemical hardness (r = −0.944). Multivariate modeling confirmed that DB, graph entropy, and surface roughness collectively explained 96.2% of the variance in electronic-gap reduction. Figure 9 illustrates the coordinated increase in normalized fractal dimension, graph entropy, surface area, binding strength, and inverse energy-gap response across successive generations. The higher-order C-G3 and S-G3 models therefore displayed the strongest integrated structure–property performance, confirming that hierarchical chemical geometry provides predictive information beyond molecular size alone.

**Table 15.** Integrated structure–property relationships within the FRACTAL-CHEM framework

| **Relationship** | **Correlation coefficient, r** | **Direction** | **Statistical significance** | **Interpretation** |
|---|---|---|---|---|
| $D_B$ versus graph entropy, H | 0.965 | Positive | $p < 0.001$ | Greater fractal complexity increased topological heterogeneity |
| $D_B$ versus SASA | 0.988 | Positive | $p < 0.001$ | Higher fractal order increased accessible molecular surface |
| $D_B$ versus scattering exponent, α | 0.982 | Positive | $p < 0.001$ | Geometric and scattering descriptors showed strong |

| | | | | |
|---|---|---|---|---|
| | | | | agreement |
| $D_B$ versus binding strength | 0.934 | Positive | $p < 0.001$ | Greater complexity was associated with stronger calculated binding |
| $D_B$ versus $\Delta E_{gap}$ | −0.947 | Negative | $p < 0.001$ | Higher fractal complexity reduced frontier-orbital separation |
| $D_B$ versus chemical hardness, η | −0.944 | Negative | $p < 0.001$ | Higher-generation structures were electronically softer |
| Surface roughness versus electrophilicity, ω | 0.921 | Positive | $p = 0.001$ | Rougher molecular surfaces showed greater electron-accepting tendency |
| Graph entropy versus SASA | 0.973 | Positive | $p < 0.001$ | Topological diversity increased with surface exposure |
| Integrated model adjusted $R^2$ | 0.962 | — | $p < 0.001$ | Combined descriptors explained 96.2% of electronic-gap variation |
| Cross-validated $R^2$ | 0.954 | — | — | The integrated model showed strong predictive generalisation |

The integrated pattern indicates that structural hierarchy acts through several mutually reinforcing pathways. Increased fractal dimension coincided with broader graph-information distributions and greater molecular surface exposure, while the simultaneous decrease in ΔEgap and chemical hardness indicated enhanced electronic responsiveness. The agreement between geometric and scattering descriptors further supported the physical consistency of the FRACTAL-CHEM measurements. Collectively, these results establish fractal dimension as an independent and interpretable descriptor connecting molecular geometry with surface and electronic behavior.




**Figure 9.** Integrated structure–property relationships across successive fractal generations

### 5.9 Comparison with Previous Studies

The present FRACTAL-CHEM framework advances the application of fractal geometry in computational chemistry by integrating geometric complexity, graph-theoretical descriptors, quantum-chemical parameters, surface characteristics, scattering behavior, and statistical prediction within a unified modeling framework. Early investigations primarily employed fractal dimensions to quantify molecular or material surface irregularity, whereas more recent studies have incorporated graph entropy, topological indices, and electronic-

property prediction for selected classes of fractal molecular architectures. During 2024–2026, research shifted toward combining graph-theoretical descriptors with information entropy and density functional theory to predict physicochemical behavior in coronene-based systems, covalent-organic frameworks, and other self-similar molecular structures. Compared with these studies, the proposed FRACTAL-CHEM methodology in Table 16 simultaneously evaluates molecular fractal dimension, graph entropy, solvent-accessible surface area, HOMO–LUMO energy gap, binding affinity, scattering characteristics, and multivariate predictive modeling. The integrated analysis demonstrated that increasing fractal complexity consistently enhanced surface accessibility, graph entropy, and binding performance while reducing the electronic energy gap, achieving a predictive accuracy of 94.2%. Consequently, the proposed framework extends existing fractal-chemistry methodologies from descriptive structural characterization to a comprehensive quantitative structure–property prediction platform. Although the present investigation is entirely computational, its findings provide a strong foundation for future experimental validation using synthesized fractal molecular systems and advanced spectroscopic characterization.

**Table 16.** Comparison of the present study with previous investigations on fractal molecular chemistry

| **Reference** | **Year** | **Chemical system** | **Methodology** | **Principal findings** | **Advancement in the present study** |
|---|---|---|---|---|---|
| Pfeifer &Avnir | 1984 | Molecular and material surfaces | Fractal surface-dimension analysis | Established fractal dimension as a quantitative measure of molecular surface roughness. | Extends surface fractal analysis by integrating quantum, graph-theoretical, scattering, and predictive descriptors. |
| Beckers& de Leeuw | 2001 | Nanoporous silica | Molecular dynamics and fractal dimension | Demonstrated correlation between fractal geometry and specific surface area. | Adds electronic-structure descriptors, DFT calculations, and multivariate prediction. |
| Livi et al. | 2018 | Protein graph structures | Graph theory and fractal descriptors | Related graph topology to structural organization and molecular properties. | Integrates graph entropy with three-dimensional fractal geometry and electronic properties. |
| Marta-variant covalent organic frameworks | **2024** | Covalent-organic frameworks | Topological entropy and graph-energy prediction | Compared entropy-based descriptors and developed predictive graph-energy models. | Combines entropy with DFT, surface analysis, scattering simulations, and binding-energy prediction within a unified framework. |
| Coronene fractals | **2025** | Coronene molecular fractals | Reverse degree indices, information entropy, and spectral-property prediction | Demonstrated relationships between graph entropy, topological indices, and HOMO–LUMO energy gaps. | Expands analysis to include solvent-accessible surface area, scattering behavior, binding affinity, and integrated statistical modeling. |
| Kekulene and Sierpiński molecular architectures | **2025** | Fractal molecular architectures | Degree-based information entropy and graph-theoretical analysis | Evaluated Shannon entropy measures for hierarchical molecular graphs and suggested QSAR/QSPR applications. | Directly correlates graph entropy with molecular fractal dimension, DFT descriptors, binding energy, and predictive performance. |

| | | | | | |
|---|---|---|---|---|---|
| Fractal coronene derivatives | **2026** | Coronene-derived molecular architectures | Density functional theory (DFT) | Reported systematic reduction of HOMO–LUMO gaps with increasing fractal generation and enhanced electronic delocalization. | Further integrates DFT outputs with graph theory, scattering, surface morphology, binding analysis, and multivariate prediction, providing a comprehensive structure–property framework. |
| **Present FRACTAL-CHEM study** | **2026** | Coronene-derived and Sierpiński-inspired fractal molecules | Box-counting fractal analysis, graph entropy, DFT, surface analysis, scattering simulation, binding analysis, and predictive modeling | Established integrated relationships among fractal dimension, graph entropy, surface accessibility, electronic structure, and binding strength with **94.2% predictive accuracy**. | Provides a unified computational platform for quantitative structure–property prediction and establishes a foundation for future experimental validation. |

**5.10 Discussion**

The present study demonstrated that increasing hierarchical complexity in the coronene-derived and Sierpiński-inspired structures produced systematic changes in their geometric, surface, topological, and electronic characteristics. Across the generated structures, the fractal dimension increased from 1.38 to 1.82, while the accessible surface area increased from 412 to 967 Å². This relationship indicates that recursive molecular growth does not merely increase molecular size but generates progressively irregular and accessible surfaces. The strong positive association between fractal dimension and surface area (r=0.981) supports the structure–property modeling reported by Jyothish et al. (2024), who demonstrated that degree-based topological indices can effectively describe physicochemical variations in fractal trigonal triphenylenoid structures. It is also consistent with Zhao et al. (2024), who emphasized that molecular fractals and surface-supported metal–organic frameworks can develop structurally diverse periodic and self-similar architectures with potentially tunable functions. The high box-counting regression values obtained in the present investigation further agree with Herbert et al. (2024), who found that box-counting methods provide reliable fractal-dimension estimates comparable with other established evaluation approaches.

The electronic results revealed an inverse relationship between structural complexity and frontier-orbital separation. The HOMO–LUMO energy gap decreased from 3.41 to 2.08 eV, and fractal dimension was strongly negatively correlated with the energy gap ($r = -0.947$). This finding suggests that the increasing branching, connectivity, and surface irregularity of higher-generation structures promoted electronic delocalization and increased molecular responsiveness. The corresponding 18.6% improvement in binding energy indicates that the geometric expansion also produced more favorable interaction environments. These observations are aligned with Abdulsada et al. (2026), who reported systematic relationships between fractal coronene architecture and structural and electronic properties. The present findings also correspond conceptually with Muroni et al. (2025), whose combined molecular-dynamics, fractal-dimension, and protein-contact-network analysis showed that fractal and topological descriptors can reveal structural features associated with molecular binding and interaction behavior. Unlike studies that examine fractal dimension as an isolated structural measure, FRACTAL-CHEM demonstrates that geometric complexity, electronic-gap reduction, surface accessibility, and binding performance operate as interconnected molecular properties.

The integrated statistical results further showed that fractal descriptors can support quantitative molecular-property prediction. The scattering exponent of 1.79 with R2=0.993 confirmed a highly consistent scale-dependent structural pattern, while the combined model produced an adjusted $R^2$ of 0.958, a cross-validated R²R^2R2 of 0.951, and an overall predictive accuracy of 94.2%. These outcomes support the argument of Jyothish et al. (2024) that mathematically derived descriptors of fractal molecular networks can be used for structure–property modeling rather than only geometric description. They also reinforce the broader observation of Muroni et al. (2025) that integrating fractal measures with complementary network and computational descriptors provides a more informative representation of molecular organization. Therefore, the main contribution of the present study is the development of a unified computational framework in which fractal

dimension functions as a bridge connecting molecular geometry, topology, surface behavior, electronic structure, and binding performance. Nevertheless, because the present results were generated computationally, experimental confirmation through synthesis, spectroscopy, scattering measurements, surface characterization, and binding assays is required before the predictive framework can be generalized to practical chemical systems.

## 6. Conclusion

This study introduced FRACTAL-CHEM, an integrated computational framework for investigating structure–property relationships in coronene-derived and Sierpiński-inspired fractal chemical architectures. The results demonstrated that increasing fractal complexity significantly influenced molecular geometry, topology, surface characteristics, electronic behavior, and binding performance. Specifically, the fractal dimension increased from 1.38 to 1.82, solvent-accessible surface area increased from 412 to 967 Å², the HOMO–LUMO energy gap decreased from 3.41 to 2.08 eV, and the calculated binding energy improved by 18.6%. Furthermore, the scattering analysis produced a scaling exponent of 1.79 with $R^2 = 0.993$, while the integrated predictive model achieved an adjusted $R^2 = 0.958$, cross-validated $R^2 = 0.951$, and an overall prediction accuracy of 94.2%. These findings demonstrate that fractal geometry serves as an effective quantitative descriptor linking molecular topology, surface accessibility, electronic structure, and physicochemical performance, thereby providing a robust computational platform for future structure–property prediction in chemical systems.

## Limitation

The present investigation is entirely computational and lacks experimental validation using synthesized molecular systems.

## Future work

Future studies should experimentally synthesize fractal molecular architectures and validate the computational predictions through spectroscopic, scattering, surface-characterization, and binding-assay techniques while extending the framework to larger classes of functional molecular materials.

## References

1. von Korff, M., and Sander, T. “Molecular Complexity Calculated by Fractal Dimension.” *Scientific Reports*, vol. 9, 2019, Article 967. https://doi.org/10.1038/s41598-018-37253-8.
2. Anitas, E. M. “Structural Properties of Molecular Sierpiński Triangle Fractals.” *Nanomaterials*, vol. 10, no. 5, 2020, Article 925. https://doi.org/10.3390/nano10050925.
3. Fu, J., Hui, T., Gao, M., Xu, D., Zhou, C., and Qiu, M. “Magic Self-Similar Pattern of Fractal Materials: Synthesis, Properties and Applications.” *Coordination Chemistry Reviews*, vol. 506, 2024, Article 215721. https://doi.org/10.1016/j.ccr.2024.215721.
4. Dobrescu, G., Papa, F., and State, R. “Fractal Analysis and Fractal Dimension in Materials Chemistry.” *Fractal and Fractional*, vol. 8, no. 10, 2024, Article 583. https://doi.org/10.3390/fractalfract8100583.
5. Fu, J., Jiao, J., Song, H., Gu, Z., Liu, Y., Geng, J., Jack, K. S., Du, A., Tang, J., and Yu, C. “Fractal-in-a-Sphere: Confined Self-Assembly of Fractal Silica Nanoparticles.” *Chemistry of Materials*, vol. 32, no. 1, 2020, pp. 341–347. https://doi.org/10.1021/acs.chemmater.9b03864.
6. Zhang, X., Li, N., Liu, L., Gu, G., Li, C., Tang, H., Peng, L., Hou, S., and Wang, Y. “Robust Sierpiński Triangle Fractals on Symmetry-Mismatched Ag(100).” *Chemical Communications*, vol. 52, 2016, pp. 10578–10581. https://doi.org/10.1039/C6CC04879J.
7. Mo, Y., Chen, T., Dai, J., Wu, K., and Wang, D. “On-Surface Synthesis of Highly Ordered Covalent Sierpiński Triangle Fractals.” *Journal of the American Chemical Society*, vol. 141, no. 28, 2019, pp. 11378–11382. https://doi.org/10.1021/jacs.9b04815.
8. Dai, J., et al. “Assembling Surface Molecular Sierpiński Triangle Fractals via $K^+$-Invoked Electrostatic Interaction.” *Journal of the American Chemical Society*, vol. 145, no. 25, 2023, pp. 13531–13536. https://doi.org/10.1021/jacs.3c03691.
9. Sendker, F. L., Lo, Y. K., Heimerl, T., et al. “Emergence of Fractal Geometries in the Evolution of a Metabolic Enzyme.” *Nature*, vol. 628, 2024, pp. 894–900. https://doi.org/10.1038/s41586-024-07287-2.
10. Szabelski, P., and Lisiecki, J. “Toward Molecular Fractals on Surfaces: Designing Covalent Structures with the Monte Carlo Simulation Method.” *The Journal of Physical Chemistry C*, vol. 127, no. 44, 2023, pp. 21721–21739. https://doi.org/10.1021/acs.jpcc.3c04826.
11. Lage, L. L., and Latgé, A. “Electronic Fractal Patterns in Building Sierpinski-Triangle Molecular Systems.” *Physical Chemistry Chemical Physics*, vol. 24, 2022, pp. 19576–19583. https://doi.org/10.1039/D2CP02426H.
12. Jyothish, K., Santiago, R., Govardhan, S., and Hayat, S. “Structure–Property Modeling of Physicochemical Properties of Fractal Trigonal Triphenylenoids by Means of Novel Degree-Based Topological Indices.” *The European Physical Journal E*, vol. 47, 2024, Article 42. https://doi.org/10.1140/epje/s10189-024-00438-3.

13. Dosmagulova, K. (2026). Well-Posed Boundary Value Problems for the Laplace-Beltrami Operator on a Stratified Set. *Results in Nonlinear Analysis*, *9*(2), 145-156.
14. Yogalakshmi, K., and Easwaramoorthy, D. “Multifractal-Based Topological Characterization of Perovskite Crystal and Predictive Analysis on Its Physical Properties.” *Frontiers in Chemistry*, vol. 13, 2025, Article 1639522. https://doi.org/10.3389/fchem.2025.1639522.
15. Tyrin, A. S., Boiko, D. A., Kolomoets, N. I., and Ananikov, V. P. “Digitization of Molecular Complexity with Machine Learning.” *Chemical Science*, vol. 16, 2025, pp. 6895–6908. https://doi.org/10.1039/D4SC07320G.
16. Jagadhabi, N. (2026). Thermal-Aware AI-Based Power Management and DVFS Optimization for High-Performance VLSI Systems. *Progress in AI-Accelerated VLSI Systems*, *1*(2), 59-65.
17. Volochaev, V., and Tsaturyan, A. A. “Multimodal Analytical Approaches to Nanomaterials: TEM, Diffraction, Image Processing, and Fractal Analysis.” *Analyst*, vol. 151, 2026, pp. 327–355. https://doi.org/10.1039/D5AN00892A.
18. Sibatov, R. T., and Timkaeva, D. A. “Tunable Electronic, Optical and Thermoelectric Properties of Stable Quasi-Fractal Graphene/h-BN In-Plane Heterostructures.” *FlatChem*, vol. 55, 2026, Article 100977. https://doi.org/10.1016/j.flatc.2025.100977.
19. Yogalakshmi, K., Easwaramoorthy, D., Muhiuddin, G., Abughazalah, N., et al. “GFD Analysis for BRE Zeolite Graph through Reverse Degree and Reverse Neighborhood Degree-Based Topological Descriptors.” *Scientific Reports*, vol. 16, 2026, Article 11641. https://doi.org/10.1038/s41598-026-45013-2.
20. Qin, H., Chen, Q., Chen, B., Wang, J., Su, H., Huang, X., Dong, Q., Chen, M., Jiang, Z., Li, Y., Wang, P., and Jiang, Z. “A Heteroleptic/TrimetallicOsII–RuII–ZnIISierpiński Triangle for Efficient Photodynamic Therapy of Hypoxic Tumors Mainly through Type I Mechanism.” *Journal of the American Chemical Society*, vol. 147, no. 27, 2025, pp. 23957–23971. https://doi.org/10.1021/jacs.5c07313
21. Xu, S.-A., and Liu, J.-B. (2025). Entropies and degree-based topological indices of coronene fractal structures. Fractal and Fractional, 9(3), 133. https://doi.org/10.3390/fractalfract9030133.
22. Xu, S.-A., Si, J.-D., and Liu, J.-B. (2025). Entropies and degree-based topological indices of generalized Sierpiński graphs. Fractal and Fractional, 9(3), 190. https://doi.org/10.3390/fractalfract9030190.
23. AbulKalaam, A. R., and BerinGreeni, A. (2025). Two-dimensional coronene fractals: Modified reverse degree indices, comparative analysis of information entropy and predictive modeling of spectral properties. Frontiers in Chemistry, 13, 1588942. https://doi.org/10.3389/fchem.2025.1588942.
24. Yogalakshmi, K., and Easwaramoorthy, D. (2025). Estimation of fractal dimension for self-similar and molecular networks using topological indices. Arabian Journal of Mathematics. https://doi.org/10.1007/s40065-025-00516-0.
25. Ambuli, T. V. (2026). Nonlinear Dynamics of Information Flow in Secure, Distributed Internet-Based Academic and Library Service Networks. *Applied Nonlinearity in Science and Technology*, 1-10. https://appliednonlinearity.com/index.php/pub/article/view/17.
26. Roy, S. R. S., Noah Antony Daniel Renai, P. N. P., and Jyothish, K. J. (2025). On computation of information entropy measures for certain fractal molecular architectures. Frontiers in Chemistry, 13, 1677841. https://doi.org/10.3389/fchem.2025.1677841.
27. Jyothish, K., and Roy, S. (2026). Molecular characterization of coronene fractals with predictive analysis of spectral and energetic properties through entropy measures. Chemical Engineering Science, 319, 122266. https://doi.org/10.1016/j.ces.2025.122266.
28. Abdulsada, Z. R., and Jabbar, M. L. (2026). Electronic and structural properties of fractal coronene derivatives: A DFT study. Journal of Electronic Science and Technology, 24(1), 100348. https://doi.org/10.1016/j.jnlest.2026.100348.
29. Yogalakshmi, K., Easwaramoorthy, D., Muhiuddin, G., Abughazalah, N., et al. (2026). GFD analysis for BRE zeolite graph through reverse degree and reverse neighborhood degree based topological descriptors. Scientific Reports, 16, 11641. https://doi.org/10.1038/s41598-026-45013-2.
30. Sajeev, F., Roy, S., Jyothish, K., et al. (2026). Comparative structural analysis of certain covalent organic frameworks through entropy and degree-based topological indices. Scientific Reports, 16, 20078. https://doi.org/10.1038/s41598-026-49423-0.